JOURNAL OF QUATERNARY SCIENCE (2023) **38**(5) 629–646 ISSN 0267-8179. DOI: 10.1002/jqs.3511

JQS Journal of Quaternary Science QRA Quaternary Research Association

Late Pleistocene and Holocene transgression inferred from the sediments of the Gulf of San Jorge, central Patagonia, Argentina

PIERRE-ARNAUD DESIAGE,[1,2,3,4]* GUILLAUME ST-ONGE,[1,3,4] MATHIEU J. DUCHESNE,[5] JEAN-CARLOS MONTERO-SERRANO[1,3] and MIGUEL J. HALLER[6,7]

[1]Institut des sciences de la mer de Rimouski, Université du Québec à Rimouski, Rimouski, QC, Canada
[2]Geological Survey of Canada (Atlantic), Dartmouth, NS, Canada
[3]GEOTOP Research Center, Montréal, QC, Canada
[4]Canada Research Chair in Marine Geology, Rimouski, QC, Canada
[5]Geological Survey of Canada (Québec), Quebec City, QC, Canada
[6]Universidad Nacional de la Patagonia San Juan Bosco (UNPSJB), Puerto Madryn, Argentina
[7]Instituto Patagónico de Geología y Paleontología – CCT CENPAT-CONICET, Puerto Madryn, Argentina

Received 5 December 2021; Revised 14 February 2023; Accepted 15 February 2023

ABSTRACT: This study presents the first detailed description of the upper sedimentary succession of the late Pleistocene and Holocene deposits in the Gulf of San Jorge (Patagonia) based on several hundred kilometers of high-resolution seismic (sparker) profiles and numerous sediment cores. High-resolution seismic stratigraphy confirms the existence of a paleo-fluvial network formed during sea-level lowstands and buried by central basin estuarine deposits during the last marine transgression. Analyses of lithostratigraphy and radiocarbon ages indicate the onset of subtidal sedimentation at ~14 cal ka BP. Before the onset of subtidal conditions, the first steps of marine incursion seem to have led to the development of lagoonal/wind–tidal flat environments, advocating for a sea-level stillstand. An abrupt increase in the log(Ti/Ca) ratio in a distinct multi-centimeter-thick layer and the identification of a wave-ravinement surface suggest rapid sea-level rise in the gulf prior to ~14 cal ka BP, consistent with Meltwater Pulse 1A. Overall, this study highlights the significant impact of sea-level rise on sedimentation in the gulf from the onset of marine incursions to the mid-Holocene, as well as the reduced contribution, as currently observed, of riverine inputs due to the progressive diminution and withdrawal of glacial drainage starting before the Holocene.

KEYWORDS: elemental geochemistry; incised valleys; MWP-1A; Patagonia; postglacial sea-level changes

Introduction

Continental shelves are key recorders of the impacts of sea-level variations during the Quaternary. They are shaped by successive subaerial erosive phases of lowstands and subsequent phases of transgression. Over recent decades, an increasing number of paleoceanographic and marine paleoclimatic studies have focused on continental shelf records rather than deep-sea archives to take advantage of the generally higher accumulation rates of sediment. However, several paleoceanographic and marine paleoclimatic studies on the outer shelf are faced with incomplete or low-resolution sedimentary records associated with short time periods and abrupt events, notably due to the distance to the primary source of sediment and because of the lower sediment accumulation rates than the inner- and mid-shelf regions (e.g., McCave, 1972; Nittrouer and Sternberg, 1981; Crockett and Nittrouer, 2004). In this context, the sedimentary records from bays and gulfs represent preferential alternatives to reconstruct late Quaternary paleoenvironmental and sea-level changes in the inner part of the continental margin. This is due to their location at the transition between the inner- and mid-continental shelf, their proximity to sediment sources and the mostly shallow waters (Perissoratis et al., 2000; Chivas et al., 2001). Furthermore, from high to mid-latitudes, large parts of these areas were located in the vicinity of ice sheets during glacial periods, allowing the preservation of sediment associated with ice sheet margin fluctuations, together with sea-level variations (e.g., Barnhardt et al., 1995; Svendsen et al., 1997; Ó Cofaigh et al., 2019).

Developed mainly on a passive continental margin and characterized by a low relief and gently dipping surface, the Argentine Continental Shelf (ACS) was greatly affected by Quaternary sea-level variations (Fig. 1a; Rabassa et al., 2005; Rabassa, 2008; Violante et al., 2014). Numerous studies have been conducted in recent decades to reconstruct the chronology of the marine transgression in the ACS, as well as the relative sea-level changes following the Last Glacial Maximum (LGM; e.g., Guilderson et al., 2000; Rostami et al., 2000; Cavallotto et al., 2004; Violante and Parker, 2004; Schellmann and Radtke, 2010; Ponce et al., 2011; Violante et al., 2014, and references therein). Based on ^{14}C dates from piston cores retrieved over the entire shelf in the 1960s, Guilderson et al. (2000) produced a post-LGM relative sea-level curve for the ACS, which was later updated and compiled by Violante and Parker (2004; Fig. 2). This sea level curve suggests that the LGM lowstand sea level occurred at ~18 ka BP at ~105 m below present sea level. The onset of the marine transgression resulted in rapid sea-level rise in the Early Holocene, with a highstand of ~6 m above present between 8 and 6 ka BP, followed by a progressive fall to its present position (Fig. 2;

*Correspondence: Pierre-Arnaud Desiage, as above.
Email: desiage.pierre.arnaud@gmail.com

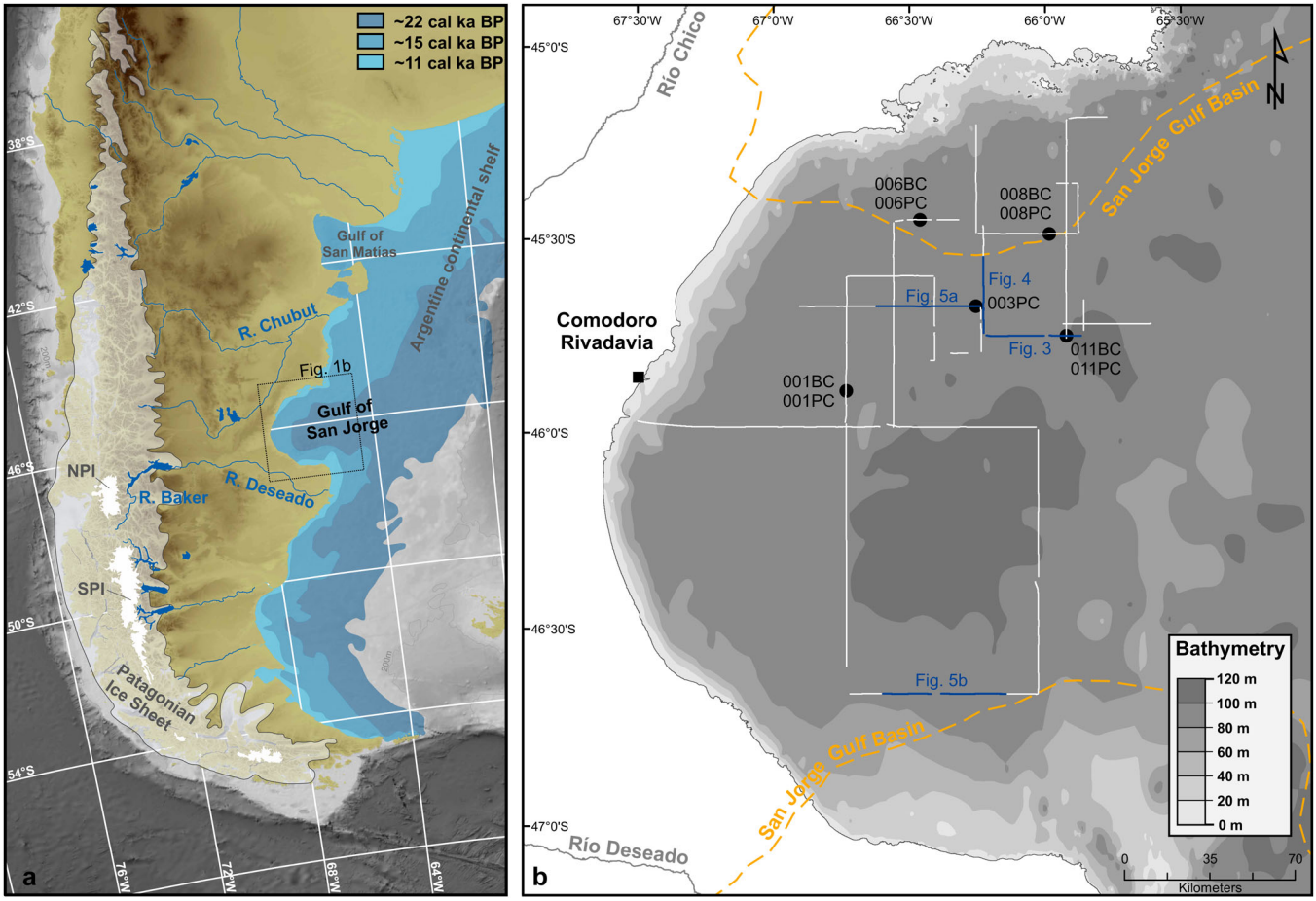

Figure 1. (a) Regional map showing the Gulf of San Jorge and the locations discussed in the text. The maximum extent of the former Patagonian Ice Sheet at the Last Glacial Maximum (LGM; adapted from Rabassa, 2008) and the location of the present-day Northern (NPI) and Southern (SPI) Patagonian icefields are illustrated in light gray and white, respectively. Also shown is the post-LGM potential position of the coastline on the Argentine Continental Shelf during the apparent stabilization of sea level from the paleogeographical model developed by Ponce et al. (2011). (b) Bathymetric map of the Gulf of San Jorge with the positions of piston cores and related box cores (black dots), as well as seismic sparker profiles (blue lines) used in this study. [Color figure can be viewed at wileyonlinelibrary.com]

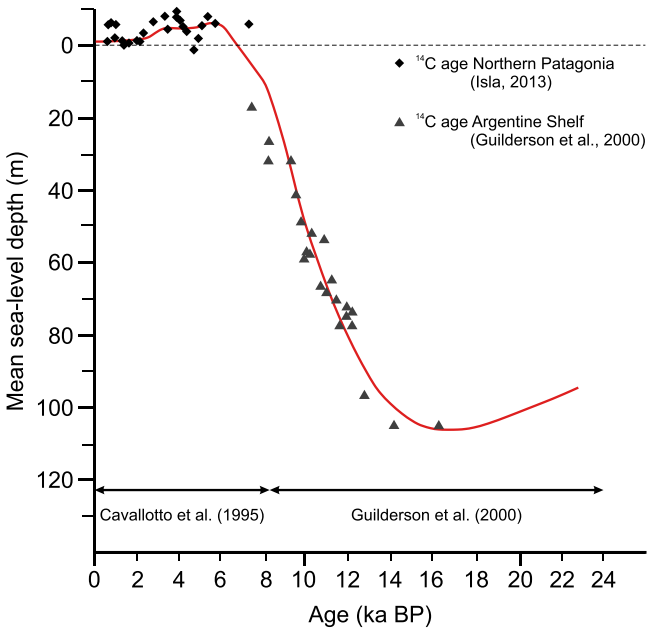

Figure 2. Post-LGM sea-level history of the Argentine Continental Shelf according to Cavallotto et al. (1995), Guilderson et al. (2000) and Isla (2013). Modified from Violante and Parker (2004). [Color figure can be viewed at wileyonlinelibrary.com]

Cavallotto et al., 2004; Milne et al., 2005; Violante et al., 2014). Despite abundant documentation on the mid- and late Holocene sea-level changes that occurred along the ACS (e.g., Cavallotto et al., 2004; Schellmann and Radtke, 2010, and references therein; Violante et al., 2014, and references therein), there is a significant lack of available sedimentological data to reconstruct the chronology of the sea-level changes prior to the mid-Holocene (Violante and Parker, 2004).

In the southern part of the ACS along the Patagonia Atlantic coast, the shore of the Gulf of San Jorge (GSJ; Fig. 1) and adjacent areas provide a suitable archive to reconstruct the Holocene sea-level history due to numerous and well-preserved littoral forms (i.e. beach ridge systems, littoral terraces and valley-mouth terraces; Schellmann and Radtke, 2010). According to the synthesis of Schellmann and Radtke (2010), relative sea level along the middle and southern Patagonian coast (including the GSJ region) reached the modern coastline at ~8.6 cal ka BP, and the Holocene transgression maximum lasted from 7.4 to 6.6 cal ka BP. After this period, the coast in the GSJ area experienced a progressive and discontinuous relative sea-level fall characterized by several phases with different rates of relative sea-level lowering (Zanchetta et al., 2012, 2014; Bini et al., 2017). Ponce et al. (2011) proposed a model for the paleogeographical evolution of the Patagonia coast since the LGM based on the global sea-level curve presented by Fleming et al. (1998), as well as maps of the recent sediment distribution

and terraces or submarine benches of the ACS proposed by Parker et al. (1997) (Fig. 1a). This model suggests that prior to the Holocene, the onset of marine flooding in the GSJ occurred at ~15.5 cal ka BP, when the water level reached ~90 m below present sea level. Apart from the work of Ponce et al. (2011) and the regional sea-level curve proposed by Guilderson et al. (2000), no investigations have attempted to reconstruct the timing of the marine transgression prior to the mid-Holocene in this sector of the ACS.

In the last 30 years, many surveys and studies have been carried out mostly in the northern part of the shelf, which have contributed to the identification of the main features of the morphostratigraphy and sedimentary sequences of the ACS from the late Pleistocene to Holocene marine transgression (e.g., Parker et al., 1997; Violante and Parker, 2004; Violante et al., 2014, and references therein). The sedimentary sequence related to post-LGM times has been estimated to be thicker than 10 m in the northern part of the shelf and thinner (<5 m) offshore Patagonia. As a large part of the ACS was subaerially exposed during the LGM, the base of the post-LGM sequence is delimited by a transgressive surface in most of the shelf (Violante and Parker, 2004; Violante et al., 2014). However, some of the pre-transgressive features have not been entirely altered by the marine transgression, and thus numerous incised valleys and channels have been preserved in the shelf, documenting the existence of paleofluvial networks during low-stand phases (Violante et al., 2014). In front of the GSJ, the morphostratigraphy of the Patagonian shelf is characterized by the presence of a partially buried drainage system, as well as three terraces covered by coarse sediments and related to phases of sea-level stabilization, in the postglacial transgression between 11 and 18 ka BP (Parker et al., 1997; Violante et al., 2014).

In this study, we present a detailed description of the upper sedimentary sequence of marine deposits in the GSJ based on high-resolution seismic stratigraphic interpretations coupled with chronostratigraphy of the post-LGM sediments and multiproxy analysis (including computerized axial tomography, magnetic susceptibility, diffuse spectral reflectance, elemental geochemistry and grain size) from five sediment piston cores. The main objectives of this study are to (i) characterize the evolution of sedimentary environments and depositional history, and (ii) document and discuss the chronology of sea-level changes since the onset of the last marine transgression in the GSJ.

Study area

The GSJ is an extension of the ACS and is considered one of the largest siliciclastic shelves in the world, with a width ranging between 170 and 850 km and a total length of 2400 km. Extending along a relatively stable continental margin on most of its surface, the shelf has mainly been conditioned by sea-level fluctuations, sediment dynamics and climatic/oceanographic processes during its evolution (Violante et al., 2014; Desiage et al., 2018). The shelf break is defined at depths that deepen to the south, from 70 to 190 m. In front of the GSJ, the depths of the shelf break range between 130 and 160 m (Parker et al., 1997; Violante et al., 2014). In the southern part of the shelf, the currents of the Patagonian section are dominated by a northward (NNE) flow of sub-Antarctic cold water conveyed onto the shelf through the Cape Horn Current and the Malvinas Current along the continental slope (Palma et al., 2008, and references therein).

Located in the central part of Patagonia between latitudes 45°S and 47°S, the GSJ forms a semicircular basin that is ~160 km long and 250 km wide, with a surface area of 39,340 km^2. The bathymetry of the gulf quickly reaches the 90-m isobath, which defines a large flat central region covering most of the surface of the gulf and corresponds to the Patagonian outer shelf (Fig. 1b; Violante et al., 2014). Moreover, the GSJ possesses a shallower elongated bank (~60 m) in its southern external part. The hydrodynamic and water mass characteristics are related to the northward circulation on the shelf and to local drivers, notably tides and strong westerly winds (Palma et al., 2008). According to a high-resolution numerical model, the mean circulation corresponds to a cyclonic gyre, which is bounded to the west by an intense coastal current and to the east by the Patagonian Current, including seasonal variability (Matano and Palma, 2018). Furthermore, the surface circulation in the GSJ is mainly driven by tidal forcing. Tides in the gulf and over the adjacent shelf are semidiurnal, with tidal amplitudes among the largest in the world, reaching ~5 m in the southern part of Patagonia and ~2 m at Comodoro Rivadavia (Panella et al., 1991; Glorioso and Flather, 1995; Palma et al., 2020). The tidal regime increases from mesotidal in the external part of the gulf to macrotidal at the western coast (Isla et al., 2002). Because of the semicircular shape of the GSJ, the fetch is less restricted than in other Patagonian gulfs; however, wave development is limited by the wind orientation coming mainly from the land (i.e., strong westerlies; Isla et al., 2006).

From a geological and geographical point of view, most of the GSJ forms the eastern part of the hydrocarbon-producing San Jorge Gulf Basin, which is surrounded by the Andean belt to the west, the North Patagonian Massif to the north and the Deseado Massif to the south. Covering an area of ~170 000 km^2, with one-third located offshore, the GSJ basin is a dominantly extensional basin that formed during the Middle Jurassic, in which Jurassic–Cretaceous sedimentary sequences are used today for oil and gas production (Figari et al., 1999; Sylwan, 2001). The GSJ basin is filled with Tertiary deposits that are mainly composed of alternating continental (including from fluvial and lacustrine depositional environments) and marine sedimentary rocks (Sylwan, 2001; Paredes, 2002). These Tertiary formations, together with the Quaternary marine and fluvio-glacial deposits (e.g., 'Rodados Patagónicos'; Martínez and Kutschker, 2011), constitute most of the tablelands and terraces overlying the GSJ basin. The tablelands reach the coast as either cliffs or coarse-clastic beach–ridge systems (Pleistocene–Holocene), and they are generally composed of gravel and/or sand (Isla et al., 2002; Schellmann and Radtke 2010, and references therein).

The gulf does not have any present-day major and perennial river tributaries that significantly affect sedimentation. The GSJ is located in the center of several hundred kilometers of coastline that lacks major rivers, except for the relatively low-flowing Deseado River (5 m^3 s^{-1}; Kokot, 2004), which reaches the ocean almost 100 km south of the GSJ. However, during the late Pleistocene and the early Holocene, the streams of the Deseado River, which drained the meltwater of the Patagonian Ice Sheet (Fig. 1a), were more significant prior to the partial reversal of the Patagonian Icefield subglacial drainage from the Atlantic to the Pacific coast (Turner et al., 2005; Kokot, 2004; Isla et al., 2015). Based on grain size, mineralogical and geochemical data as well as a sediment unmixing model, Desiage et al. (2018) suggested that the origins of surface sediments in the GSJ, dominated by fine to medium silt, were 50% from external/oceanic inputs, 40% from inner gulf shores (i.e. erosion and runoff) and 10% from dust (i.e. eolian transport).

Method

The data used in this study were collected onboard the R/V *Coriolis II* in 2014 as part of the PROMESSe (PROgrama

Multidisciplinario para el Estudio del ecosistema y la geología marina del golfo San Jorge y las costas de las provincias de Chubut y Santa Cruz) project. The geophysical survey consisted of hundreds of kilometers of high-resolution seismic data acquired in the GSJ and on the shelf in front of the gulf using a sparker system (Figs. 1, 3, 4 and 5). Based on seismic data analysis, five piston cores (PCs; Fig. 6) and accompanying trigger weight cores (TWCs), 10 gravity cores (GCs) and eight box cores (BCs) were recovered from the GSJ. This paper focuses on a combination of sparker seismic data and piston cores, with a focus on four selected cores: 003PC, 006PC, 008PC and 011PC (Figs. 1b and 6; Table 1). Only the first

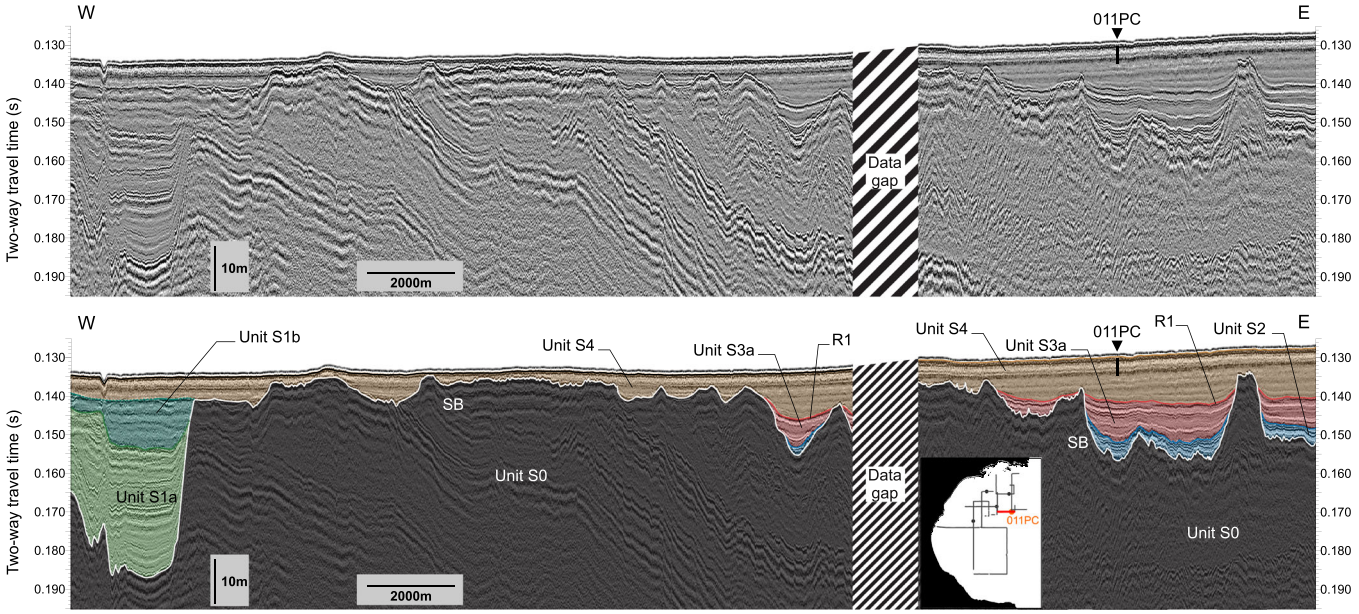

Figure 3. High-resolution sparker seismic profile (section of Line 018; top), with the interpreted version (base) showing six seismic units and subunits (units S0, S1a, S1b, S2, S3a and S4) and the location of core 011PC. The section of Line 018 that is shown is marked by a red line on the enclosed map. [Color figure can be viewed at wileyonlinelibrary.com]

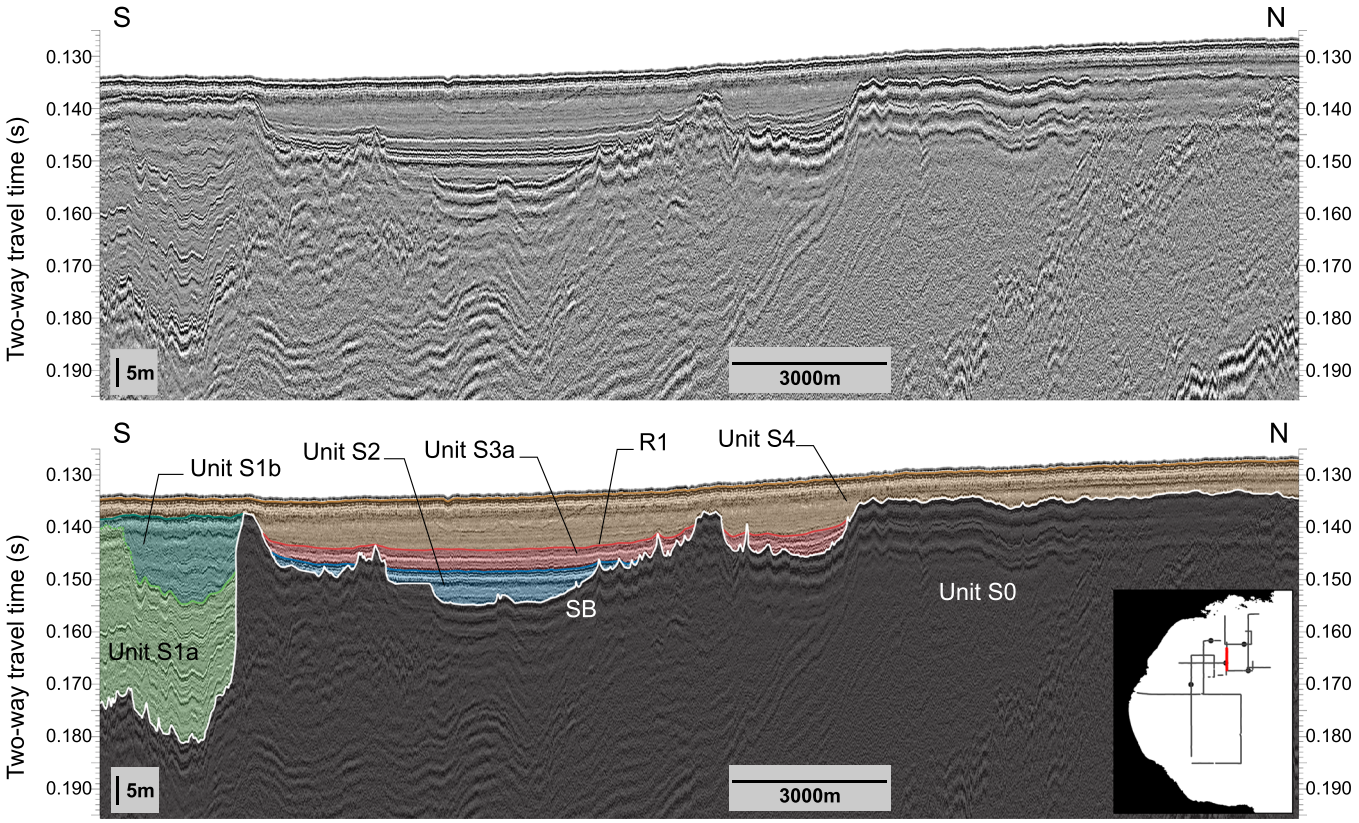

Figure 4. High-resolution sparker seismic profile (section of Line 017; top), with the interpreted version (base) showing six seismic units and subunits (units S0, S1a, S1b, S2, S3a and S4). The section of Line 017 that is shown is marked by a red line on the enclosed map. [Color figure can be viewed at wileyonlinelibrary.com]

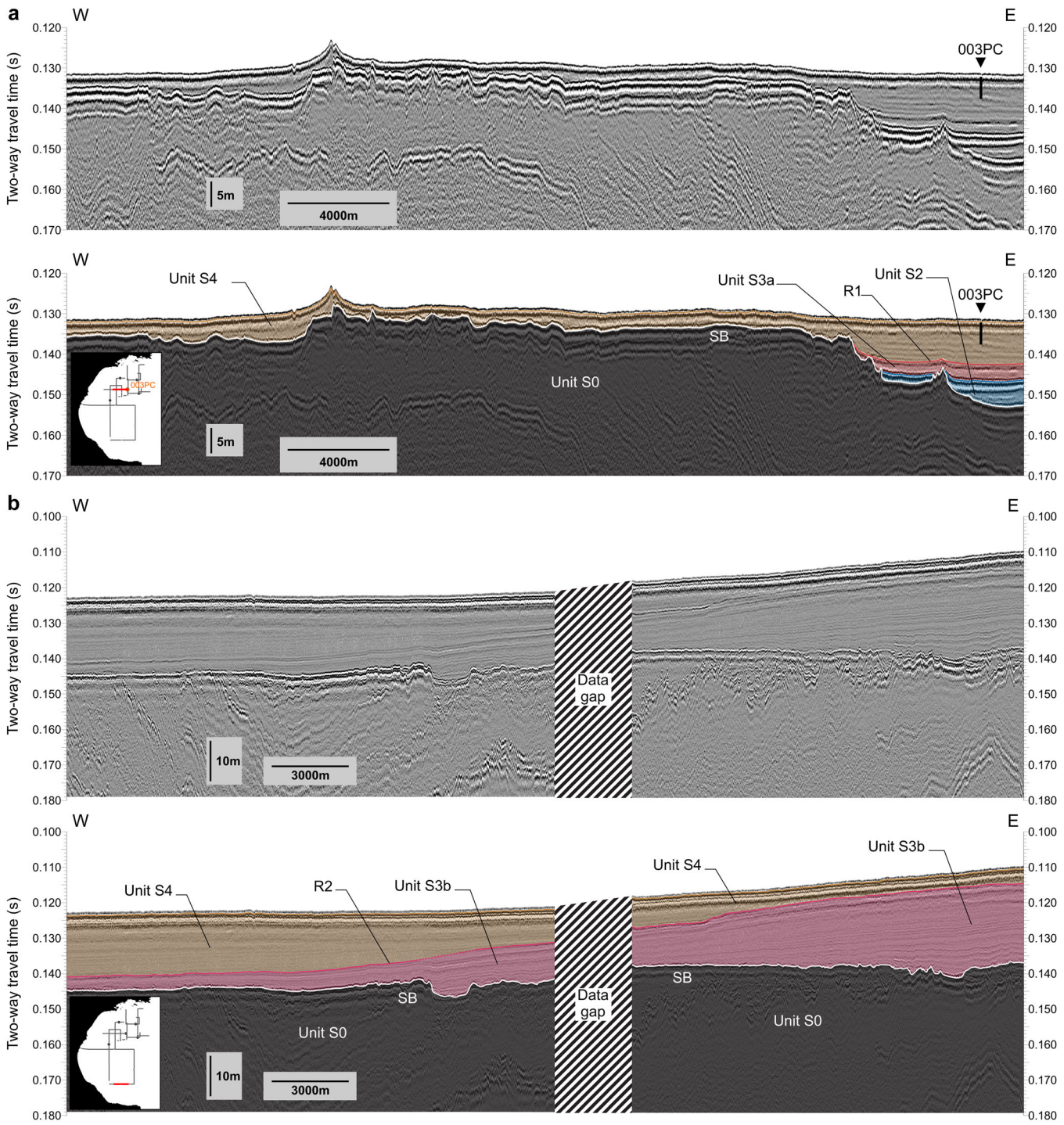

Figure 5. (a) High-resolution sparker seismic profile (section of Line 008; top), with the interpreted version (base) showing four seismic units and subunits (units S0, S2, S3a and S4) and the location of core 003PC. (b) High-resolution sparker seismic profile (section of Line 003; top), with the interpreted version (base) showing three seismic units and subunits (units S0, S3b and S4). The sections of Lines 008 and 003 that are shown are marked by a red line on the enclosed map. [Color figure can be viewed at wileyonlinelibrary.com]

230 cm of core 006PC was used in this study because of the absence of any datable material in the lower part of the core, as well as the presence of an erosional contact dividing two distinct lithological units between the dated and undated sections. The physical and geochemical properties of the box cores were used to ensure that the top sediments in the piston cores were preserved (Supporting Information, Fig. S1).

Geophysical surveys and data processing

The high-resolution sparker data were collected with an Applied Acoustics Squid 2000 sparker array shooting at an interval of 1 s (~3 m), with an output energy between 1000 and 1500 J. The acoustic signal was recorded with a 12-element, 50-m-long single-channel streamer. Sparker raw data were processed with Schlumberger's VISTA commercial seismic processing package. The processing procedure included swell correction, Butterworth bandpass filtering, minimum-phase spiking deconvolution, scaling correction, automatic gain control and trace mixing (Duchesne and Bellefleur, 2007; Duchesne et al., 2007). The application of this processing routine allowed effective attenuation of the artifacts related to strong secondary arrivals inherent to sparker sources (Mosher and Simpkin, 1999). However, a ringing pattern persisted close

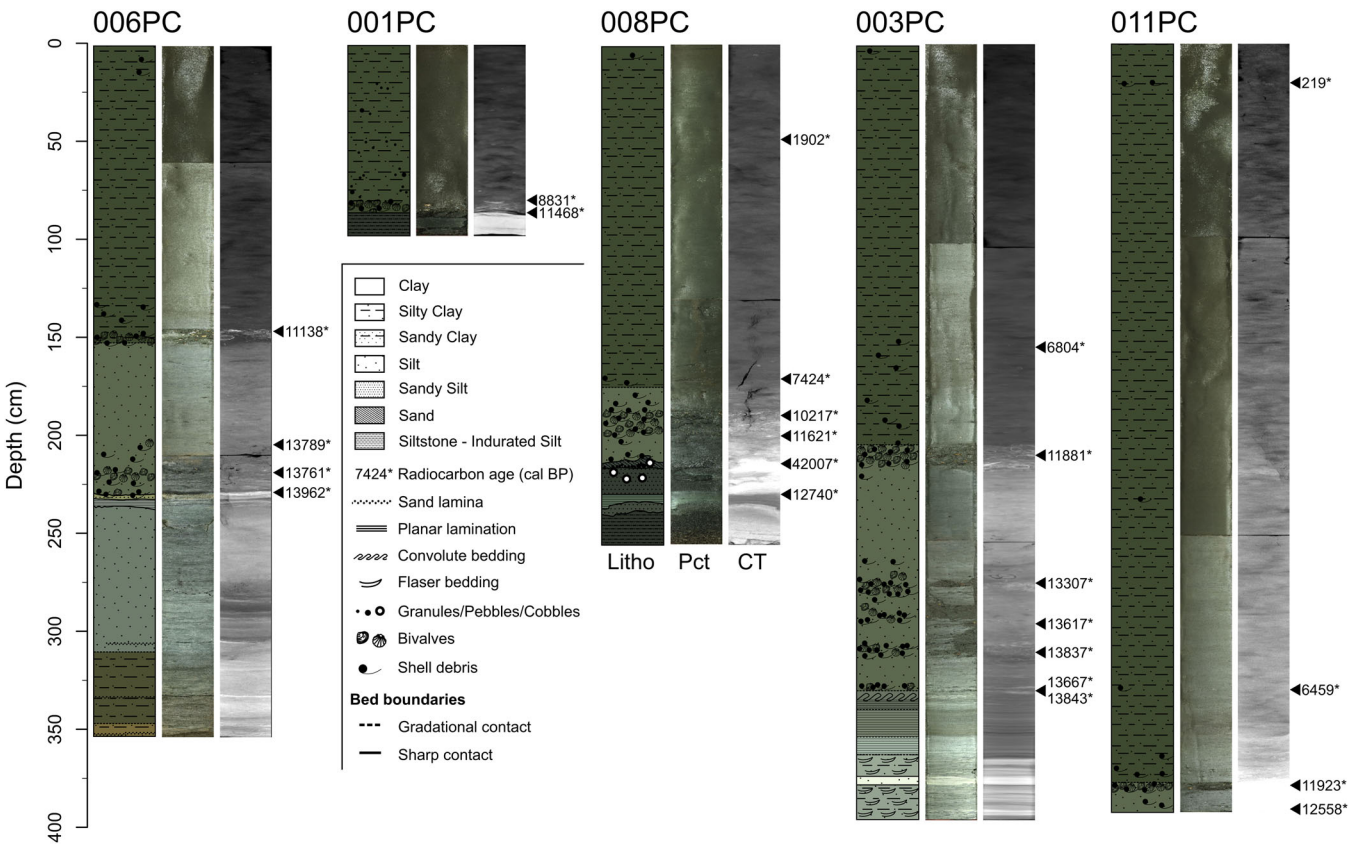

Figure 6. Lithological descriptions (Litho), photographs (Pct), CT-scan images (CT) and calibrated radiocarbon ages from piston cores retrieved from the GSJ during the 2014 expedition. [Color figure can be viewed at wileyonlinelibrary.com]

Table 1. Location, water depth, length and piston cores retrieved from the GSJ during the MARGES expedition.

Core	Longitude (°W)	Latitude (°S)	Water depth (m)	Length (cm)*	Samples
COR1404-001PC	66.734	45.907	101	103	15
COR1404-003PC	66.255	45.674	94	411	62
COR1404-006PC	66.461	45.450	91	369	62
COR1404-008PC	65.984	45.486	95	271	48
COR1404-011PC	65.924	45.750	97	406	49

*Length of the whole core measured on the vessel.

to the seafloor interface, thus reducing the vertical resolution as well as restricting interpretations for the uppermost section. The processed seismic data were then integrated and analyzed with IHS Kingdom commercial seismic and geological interpretation software. Acoustic travel times were converted into depths by using an average seismic velocity of 1480 m s^{-1} in the water column and 1540 m s^{-1} in the sedimentary deposits according to previous values for the Quaternary deposits of the ACS (Kostadinoff, 1992).

Physical and geochemical properties of sediment cores

The whole core sections were first analyzed for wet bulk density obtained by gamma ray attenuation and volumetric magnetic susceptibility (k_{LF}) at 1-cm intervals using a GEOTEK Multi-Sensor Core Logger (MSCL). Digital X-ray images of sediment cores were also obtained with a CT scan (computerized axial tomography) at INRS-ETE (Québec City). The cores were then split, described and photographed (Fig. 8). Diffuse spectral reflectance measurements (sediment color) were carried out on split core sections using a Minolta CM-2600d spectrophotometer and then converted into the L^*, a^*, b^* (L^*: lightness; a^*: green-to-red scale; b^*: blue-to-yellow scale) color space of the CIE (International Commission on Illumination). Chemical composition was determined using an energy-dispersive Olympus Innov-X DELTA portable X-ray fluorescence (pXRF) analyzer integrated with the MSCL and equipped with a 40 kV rhodium anode X-ray tube. The color reflectance, XRF and refined magnetic susceptibility measurements were performed at 0.5-cm and 1-cm intervals for the box cores and piston cores, respectively. Prior to grain size analysis, the five piston cores were evenly sampled every 8 cm with refined sampling at 4-cm intervals for basal sections of cores 003PC, 006PC and 008PC (total of 236 samples).

Grain size analysis of sediment samples was carried out on the detrital fraction using a Beckman Coulter LS 13 320 particle size analyzer (0.04–2000 μm). Deflocculation was performed by successive washing with distilled water, and the samples were mechanically shaken for 12 h before measurement. Grain size distribution and statistical parameters were processed with GRADISTAT software (Version 8.0) using the geometric (μm) and logarithmic (φ) method of moments (Blott and Pye, 2001).

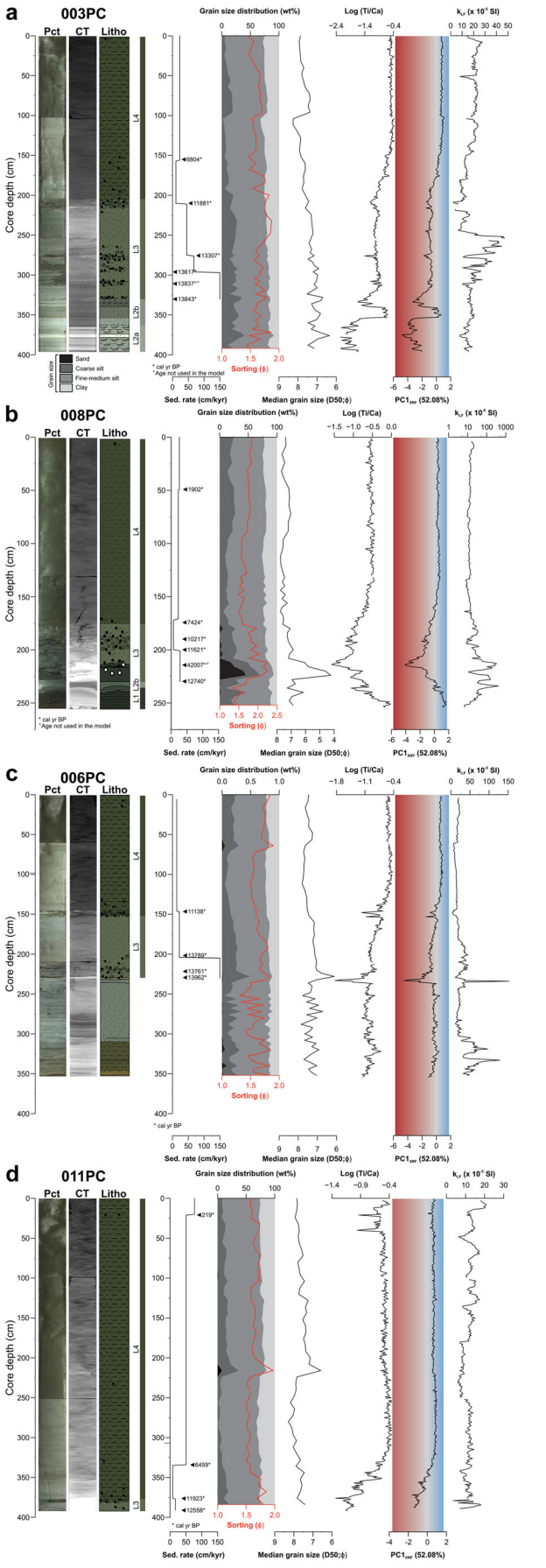

Figure 7. Grain size and elemental geochemical composition, magnetic susceptibility and sedimentation rate coupled with photographs, CT-scan images, lithological description, lithofacies and calibrated radiocarbon ages of the investigated piston cores 003PC (A), 006PC (B), 008PC (C) and 011PC (D). [Color figure can be viewed at wileyonlinelibrary.com]

Based on principal component analysis (PCA) of the pXRF data (Fig. S2), we selected the log(Ti/Ca) ratio to monitor past changes in terrigenous detrital content relative to marine carbonates (Blanchet et al., 2009; Tjallingii et al., 2010; Rothwell and Croudace, 2015). The origin of Ti in sediments is commonly associated with inputs of terrigenous continental material, whereas a substantial part of Ca is generally related to biogenic inputs, so the Ti/Ca ratio can record the relative variations in terrigenous clastic inputs and marine carbonates (e.g., Tjallingii et al., 2010; Rothwell and Croudace, 2015; Li et al., 2019). The Ti/Ca ratio is presented as a log ratio to mitigate the amplitude changes in elemental concentrations caused by variable water content, grain size distribution and irregularities of the split core surface (Weltje & Tjallingii, 2008).

The elemental composition analysis of sample 003PC-AB-376 was performed using an INCA X-sight energy dispersive X-ray spectrometer (Oxford Instruments) coupled to a JEOL 6460LV scanning electron microscope. X-ray spectra were measured from 10 randomly chosen particles, with two or three spectra per particle (Fig. S3). Each spectrum was acquired for 120 s of live time at an accelerating voltage of 20 kV. System quantitative optimization was made using copper as a standard.

Radiocarbon dating

Twenty-two samples of bivalve shells (complete or fragments) from the five piston cores were dated by ^{14}C accelerator mass spectrometry (AMS) at the Keck-Carbon Cycle AMS facility (University of California, Irvine). The samples were previously prepared and pretreated at the Radiochronology Laboratory of the Centre d'études nordiques (Laval University). Furthermore, two samples of microfragments of algae and wood were dated by ^{14}C AMS at the Laboratoire des sciences du climat et de l'environnement (LSCE, CNRS-CEA-UVSQ). The microfragments were retrieved in sieved sediment from two 1-cm sections of core 06PC (49–50 and 231–232 cm). Radiocarbon ages were calibrated using CALIB version 7.1 software (Stuiver and Reimer, 1993) and the Marine13 calibration curve (Reimer et al., 2013). Due to the evolution of depositional environments in the sediment cores and the uncertainties regarding post-LGM ^{14}C-reservoir values of the extensive Atlantic coast of Argentina (Gómez et al., 2008; Schellmann and Radtke, 2010), two different values of marine regional reservoir correction (ΔR) were applied: (i) $\Delta R = 0$, as suggested and used for mollusk shells in coastal environments of the GSJ area (Cordero et al., 2003; Schellmann and Radtke, 2010); and (ii) $\Delta R = 200$, as used by Guilderson et al. (2000) for the Argentine Shelf and based on the ^{14}C reservoir value (R) of ~560–600 years for the Falkland current (Broecker and Olson, 1961). Conventional and calibrated ages are presented in Table 2. The calibrated ages are suggested according to their ±2 sigma range (95% degree of confidence).

Prior to the construction of age–depth models, the correlation of physical and geochemical parameters measured on the piston cores and their related box cores (i.e. retrieved at the same site) were conducted to estimate the absence and deformation of sediments at the top of the piston cores (Fig. S1). To compensate for the absence of a box core at the site of core 003PC, as well as the overpenetration of the companion trigger weight core that was noted during the expedition, this core was correlated with the closest 'depth-corrected' piston core, 011PC. The correlation suggests that, except for core 008PC, in which 2 cm is missing, no sediments were lost due to coring at the top of cores 003PC, 006PC and 011PC. The deformation of muddy sediments in the uppermost parts of cores 006PC, 008PC and 011PC, related to the cumulative action of compaction and stretching during piston coring, is estimated to be ~4.5, 3 and 2 cm, respectively.

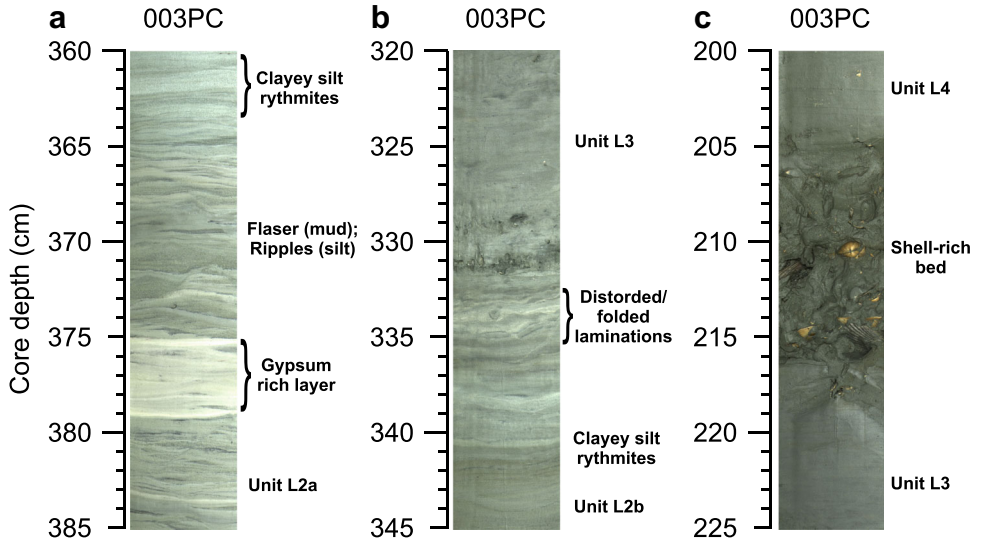

Figure 8. Photographs of unit L2a (A), the contact between L2b and L3 (B), and the transition between units L3 and L4 (C) in core 003PC. [Color figure can be viewed at wileyonlinelibrary.com]

According to these results, the depths of the piston cores have been adjusted, and the age–depth models for cores 003PC, 006PC, 008PC and 011PC have been generated using corrected depths. Finally, no significant correlations have been found between the short piston core 001PC and the first 35 cm of 001BC, which might suggest that at least 35 cm is missing at the top of 001PC. For this reason, and due to the configuration of the core and the lack of available ^{14}C dates, no age–depth model was generated for core 001PC. According to these results, which seem to imply that the tops of the piston cores represent the actual sedimentation (i.e. no/little missing sediment), age–depth models have been constructed by considering the tops of the cores as modern ages.

In this paper, the corrected depths for piston cores 003PC, 006PC, 008PC and 011PC were used only for the development of age models. The 'best-fit' linearly interpolated age–depth models were constructed using the Bayesian statistical approach of the BACON v2.2 package of R software (Fig. 9; Blaauw and Christen, 2011). The age–depth models were generated using a marine regional reservoir correction (ΔR) of 0 to compare and discuss the chronostratigraphic records that were previously published for the GSJ area (e.g. Schellmann and Radtke, 2010).

Results and interpretations

Seismostratigraphy

Five seismic units, including the acoustic basement, have been identified in the uppermost succession of the offshore sedimentary sequence in the GSJ. The five seismic units introduced below are labeled from oldest to youngest. Description and interpretation of the seismic units are made in accordance with the standard procedures of seismic stratigraphy (e.g. Mitchum et al., 1977; Sangree and Widmier, 1979).

Unit S0 – Acoustic basement

Unit S0, which is considered in this paper to be the acoustic basement, is characterized by a series of high- to moderate-amplitude reflections interspersed by transparent intervals. The configuration of the seismic reflections varies from subparallel and wavy in the central part of the GSJ (Figs. 3 and 4) to oblique in the northern, southern and external sectors (Fig. 5). The surface of the unit is defined by a high-amplitude reflection that alternately forms a smooth mounded erosional surface and irregular incised erosional truncations, marking an angular unconformity between S0 and younger seismic units. This erosional surface SB forms channels and valleys that are observed mainly in the central–external part of the gulf (Figs. 3, 4 and 5a). The acoustic basement crops out at the seafloor ~10 km off Comodoro Rivadavia in the western part of the GSJ, as well as ~40 km off the coast of the Patagonia Austral Marine Park in the northern area.

According to previous investigations of the terrestrial GSJ basin stratigraphy, which are based on outcrop and well log descriptions, as well as seismic profile analysis, we hypothesize that unit S0 is composed of mid-Cenozoic sedimentary successions, including the uppermost Santa Cruz and Chenque (Patagonia) Formations (Bellosi, 1990; Nullo and Combina, 2002; Paredes, 2002). Furthermore, similar seismostratigraphic characteristics, with a distinct discordance between Miocene and Pleistocene/Holocene deposits, have been previously observed ~500 km north of the GSJ in the gulf of San Matias (Mouzo, 2017). Unit S0 would thus correspond to the Miocene marine–estuarine deposits (Chenque Formation), which are mainly composed of sandstones interbedded with claystones, and they are transitionally overlain by fluvial deposits (Santa Cruz Formation) characterized by sandstone and claystone beds (Nullo and Combina, 2002; Paredes, 2002). The surface SB is interpreted as an erosional unconformity that was initiated during pre-transgressive times when the GSJ was exposed to subaerial conditions.

Units S1

Units S1a and S1b were identified only along three seismic lines (Figs. 3 and 4), and they fill the deepest incised structure observed in the gulf. These units consist of low- to high-amplitude (unit S1a) and low- to moderate-amplitude (unit S1b) concave up to wavy or subparallel reflections. The seismic terminations onlap against the incised structure walls (Fig. 4). The geometry of these units is characterized by a divergent configuration, with a combined maximum thickness of deposits of ~35 m in the deepest part of the depression. Unit S1b covers unit S1a, and its upper boundary corresponds to a

Table 2. Radiocarbon ages from the piston cores analyzed in this study. All ages were calibrated using CALIB version 7.1 software (Stuiver and Reimer, 1993) with the Marine13 calibration curve (Reimer et al., 2013) and two different values of ΔR (0 and 200; see details in the Radiocarbon dating section). Calibrated ages are presented with their minimum, maximum and median values.

Core	Depth in the core (cm)	Corrected depth (cm)	Lithology	Material	^{14}C age (uncalibrated)	^{14}C cal BP (2 sigma; ΔR = 0*)	^{14}C cal BP (2 sigma; ΔR = 200*)	Lab. ID
001PC	81		Olive gray silty clay (L4)	Shell fragment	8275 ± 25	(8698–8957) 8831	(8439–8600) 8531	UCIAMS-163922
001PC	86		Shell bed (L4)	Shell fragment	10400 ± 25	(11276–11701) 11468	(11118–11260) 11192	UCIAMS-163923
003PC	155.5	155	Olive gray silty clay (L4)	Shell fragment	6340 ± 25	(6718–6890) 6804	(6484–6651) 6574	UCIAMS-163005
003PC	210.5	210	Shell bed (L3)	Bivalve shell	10580 ± 25	(11713–12026) 11881	(11249–11660) 11415	UCIAMS-163004
003PC	275	274.5	Shell bed (L3)	Bivalve shell	11835 ± 35	(13205–13409) 13307	(12994–13253) 13133	UCIAMS-163915
003PC	296	295.5	Light olive gray clayey silt (L3)	Bivalve shell	12170 ± 25	(13482–13749) 13617	(13317–13507) 13412	UCIAMS-163000
003PC	310	309.5	Shell bed (L3)	Bivalve shell	12360 ± 30	(13719–13966) 13837	(13470–13743) 13605	UCIAMS-163914
003PC	330	329.5	Light olive gray clayey silt (L3)	Shell fragment	12210 ± 35	(13511–13803) 13667	(13334–13561) 13446	UCIAMS-163912
003PC	330	329.5	Light olive gray clayey silt (L3)	Shell fragment	12365 ± 30	(13724–13971) 13843	(13475–13749) 13611	UCIAMS-163921
006PC	13	17	Olive gray silty clay (L4)	Bivalve shell	Modern			UCIAMS-163908
006PC	146	150.5	Shell bed (L4)	Bivalve shell	10125 ± 20	(11054–11210) 11138	(10745–11028) 10888	UCIAMS-194470
006PC	204	208.5	Light olive gray clayey silt (L3)	Shell fragment	12315 ± 25	(13665–13911) 13789	(13436–13686) 13556	UCIAMS-163006
006PC	219	223.5	Shell bed (L3)	Bivalve shell	12290 ± 30	(13626–13888) 13761	(13411–13666) 13529	UCIAMS-163916
006PC	230	234.5	Light olive gray clayey silt (L3)	Shell fragment	12480 ± 30	(13834–14089) 13962	(13612–13877) 13749	UCIAMS-163019
008PC	49	47.5	Olive gray silty clay (L4)	Algae/wood micro-fragments	2290 ± 50‡	(1772–2043) 1902	(1541–1801) 1666	GifA17577a
008PC	171	169.5	Olive gray silty clay (L4)	Shell fragment	6910 ± 20	(7367–7478) 7424	(7169–7298) 7240	UCIAMS-163913
008PC	190	188.5	Shell bed (L3)	Bivalve shell	9390 ± 25	(10162–10287) 10217	(9885–10124) 10004	UCIAMS-163911
008PC	200	198.5	Light olive gray clayey silt (L3)	Shell fragment	10470 ± 25	(11372–11828) 11621	(11166–11344) 11247	UCIAMS-163926
008PC	214	212.5	Mass wasting deposit (L3)	Shell fragment	38060 ± 400	(41417–42567) 42007	(41255–42449) 41872	UCIAMS-163920
008PC	231	229.5	Laminated clayey silt (L2b)	Wood/Algae micro-fragments	11270 ± 50†	(12643–12848) 12740	(12517–12706) 12609	GifA17578a
011PC	20	17	Olive gray silty clay (L4)	Bivalve shell	575 ± 20	(137–275) 219		UCIAMS-163925
011PC	334	332	Olive gray silty clay (L4)	Shell fragment	6045 ± 20	(6391–6537) 6459	(6198-6312) 6264	UCIAMS-163924
011PC	378	376	Shell bed (L3)	Bivalve shell	10605 ± 20	(11774–12045) 11923	(11289-11702) 11477	UCIAMS-163007
011PC	391	389	Light olive gray clayey silt (L3)	Shell fragment	10990 ± 25	(12473–12634) 12558	(12074-12450) 12264	UCIAMS-162999

*Calibrated with Marine13 and CaliB; reservoir correction factor is the global mean of 400 years.
†1 sigma.

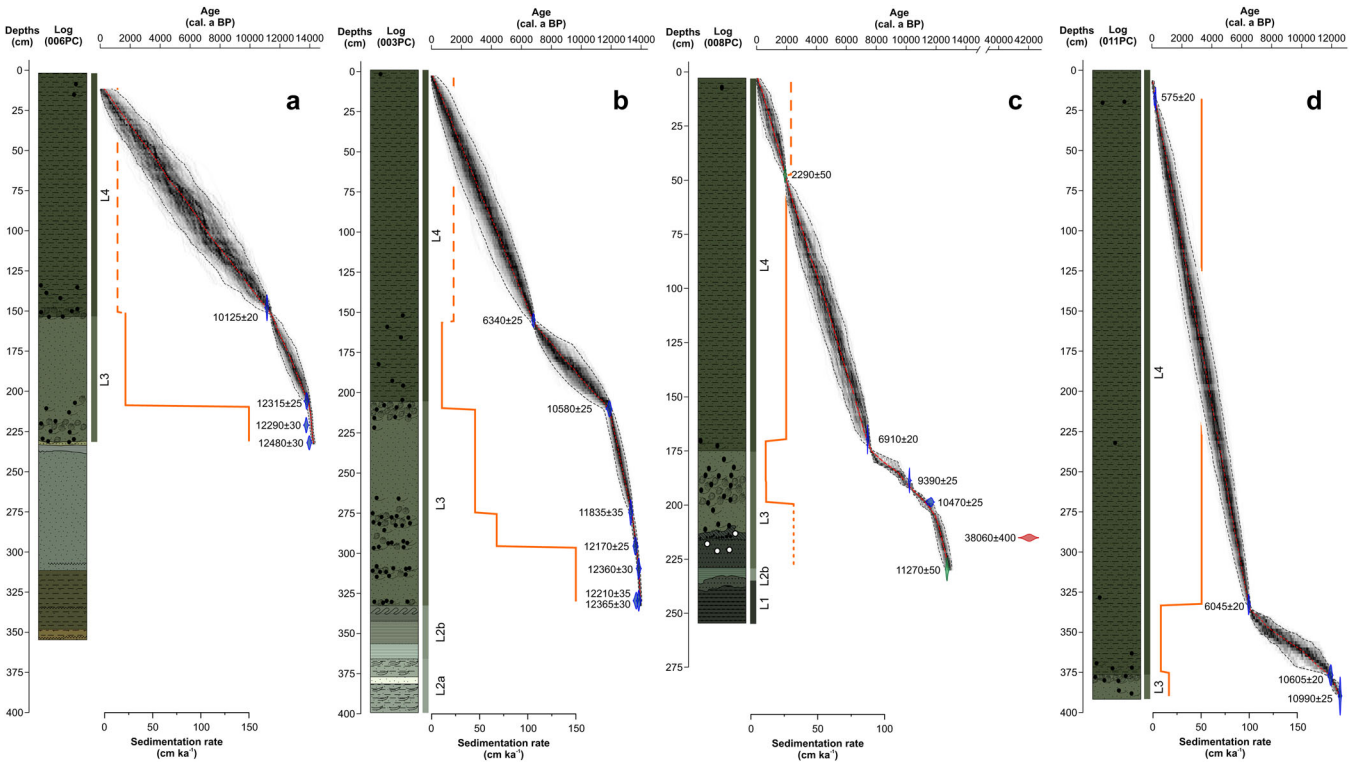

Figure 9. Age–depth models for cores 006PC (A), 003PC (B), 008PC (C) and 011PC (D), generated with the BACON package of R software (Blaauw and Christen, 2011). Calibrated radiocarbon ages used in the age–depth models are presented in transparent blue, except for the AMS ^{14}C ages from microfragments of algae and wood, and the age from 008PC not retained, which are shown in transparent green and red, respectively. Calibrated radiocarbon dates are also illustrated with their respective uncalibrated conventional ages. The gray dotted lines correspond to the 95% confidence intervals, and the red dotted line shows the 'best' model based on the weighted mean age for each depth. Sedimentation rates are presented with orange lines. Their upper sections, where the age–depth models have been constructed considering the top of the cores as modern, are dashed lines, and the lowermost section of unit L3 in 008PC, where radiocarbon age inversion suggests a reworked deposit, is shown as a dotted line. [Color figure can be viewed at wileyonlinelibrary.com]

slightly irregular surface that intersects the top of the valley banks.

Observed solely in the deepest incised structure, the acoustic configuration of units S1a and S1b, with low to moderate amplitudes, as well as confined continuous reflections, suggests central basin fine-grained deposits associated with wave-dominated and mixed wave- and tide-dominated estuaries (Zaitlin et al., 1994; Allen and Posamentier, 1994). Similar seismic units have been previously observed and described on the French Atlantic coast (e.g., Weber et al., 2004; Menier et al., 2006; Chaumillon et al., 2008), on the New Jersey shelf (Nordfjord et al., 2006) and in South Africa (continental shelf: Green, 2009; Green et al., 2013; Lake St Lucia: Bernallack et al., 2016; Dladla et al., 2019). The slightly transparent appearance with weaker reflections of S1b implies more homogeneous deposits. This suggests an evolution of the depositional environment related to sea-level rise and/or changes in other forcing parameters, such as river discharge and sediment supply. However, the interpretation of the depositional environments of units S1 is relatively speculative and cannot be corroborated by lithostratigraphic analysis due to the absence of sediment cores intersecting the seismic units.

Units S2 and S3

The internal configuration of unit S2 consists of wavy-to-subparallel, low- to moderate-amplitude reflections (Figs. 3, 4 and 5a). The seismic terminations onlap against the valley walls. Its base unconformably overlies the surface of acoustic basement S0. In the gulf, unit S2 is present exclusively in the deepest incised channels and valleys, except for the depression filled by units S1, in which its maximal thickness reaches ~5 m.

Units S3a and S3b are characterized by low- to medium-amplitude reflections and appear as semitransparent acoustic facies (Figs. 3–5). Unit S3a is also observed in the deepest incised structures overlying unit S2, as well as on acoustic basement S0 in shallower depressions. The configuration of S3a shows confined subparallel, laterally continuous seismic reflections, as well as occasional oblique subparallel reflections in shallower incised structures (Fig. 4). In the channels and valleys, the basal surface of S3a is concordant with S2, and when the latter is absent, S3 unconformably overlies S0. As observed for S2, the seismic terminations onlap against the incised structure walls. The thickness of this unit ranges from <1 to 10 m in these depressions. Seismic unit S3b was observed in the southern–external study area of the gulf, where its maximum thickness can reach ~17 m at the depocenter (Fig. 5b). In this sector, the slightly downlapping seismic reflections of S3b present a sigmoidal configuration, forming a large-scale, slightly mounded (i.e. convex-upward) morphology.

The interpretation of units S2 and S3 is also based solely on the analysis of their reflection characteristics because these units have not been reached by piston cores. The aspect and configuration of units S2 and S3a observed in incised structures suggest valley fill deposits. According to the low- to moderate-amplitude continuous reflections, as well as the distinct onlap against the edges of incised structures, we propose that seismic units S2 and S3 could correspond, as for S1a and S1b, to the filling of paleochannels by fine-grained central basin deposits associated with wave-dominated and mixed wave- and tide-dominated estuaries (Zaitlin et al., 1994;

Allen and Posamentier, 1994). Seismic unit S3a shows a similar acoustic configuration to S1b, as it is characterized by low-amplitude and symmetric reflections with seismic termination onlaps against incised valley walls. This suggests a change in depositional regime related to the progression of marine transgression and/or the evolution of sediment supply.

In the southwestern part of the GSJ, the limited distribution of unit S3b indicates that sedimentary processes affected only this sector of the gulf. The sigmoidal configuration of medium-amplitude reflections and the laterally elongated configuration of S3b advocate that the deposition of this unit was controlled by predominant hydrodynamic factors. Indeed, the deposits associated with unit S3b show seismic characteristics similar to morphological features, such as large sand bodies (Dyer and Huntley, 1999; Liao et al., 2008) or shallow-water bottom current sand deposits (Viana et al., 1998) that formed as a result of strong predominant or combined currents (e.g. geostrophic, longshore and tidal currents). Furthermore, this morphological feature seems to coincide with a shallow bank facing NNE, which divides the southern part of the GSJ from the shelf (Fig. 1). The development of these deposits could thus be linked to the transport of coarse sediments by strong NE longshore currents (Matano and Palma, 2018) originating from the Deseado River, which is located almost 100 km south of the GSJ, at a time when its flow was more significant (Kokot, 2004; Isla et al., 2015). However, since unit S3b is observed only on two perpendicularly intersecting seismic lines, it is difficult to characterize and delimit and thus to define the mechanisms behind its deposition.

Unit S4

Unit S4 is mostly semitransparent and has few low-amplitude subparallel reflections. In most of the GSJ, unit S4 unconformably overlies the acoustic basement, S0. The basal surface of S4 is separated from S3a by a smooth moderate-amplitude reflector (R1) that shows limited angular unconformities between these seismic units in the deepest incised structures. In the southern–external area of the gulf, unit S4 overlies S3b, and its base is characterized by onlap terminations and defined by a low-amplitude reflector (R2). The surface of unit S4 corresponds to most of the present-day seafloor in the GSJ. Its thickness varies from <1 m to ~8 m in the deepest incised valleys, but its maximum thickness is observed in the southern–external part of the GSJ, where it can reach ~13 m.

With the exception of the acoustic basement, S4 is the only seismic unit that has been reached by sediment cores (Figs. 3, 5 and S4). According to the lithologic and chronostratigraphic interpretation of these sedimentary records, the upper part of S4 corresponds to deposits of the last marine transgression, as well as Holocene hemipelagic sedimentation (see 'Lithostratigraphy' below). However, in several sectors of the GSJ, in which more accommodation space was available, significant sections of the basal part of S4 were not reached by sediment cores (Figs. 3, 5 and S4). Thus, in the absence of complete recovery of the sedimentary records of the thickest part of unit S4, it remains unclear whether S4 corresponds solely to deposits that have been deposited since the last marine transgression or to deposits from older sedimentary environments, such as previous Quaternary marine transgressions. However, multiple sea-level cycles would be exhibited by erosional reflectors, illustrating potential subaerial exposures associated with lowstand periods. The seismic architecture of unit S4 presents inconsequential evidence of aggradation and/or progradation, even though the unit includes at least the sedimentary deposits of the last marine transgression. This could be explained by the relative equilibrium between sediment supply and eustatic sea-level changes in a passive, relatively stable continental margin (Galloway, 1989). This configuration could possibly have been amplified by the shallow semi-enclosed morphology of the gulf, as well as moderate sediment inputs in the GSJ during the Holocene. This low sediment input is due to the almost total absence of major perennial tributaries in this sector of Patagonia that are likely to supply the gulf with terrigenous material (Kokot, 2004; Isla et al., 2015; Desiage et al., 2018). Due to the transgressive infilling context of the valley, the seismic expression and its confinement to incised features, R1 has been interpreted as a tidal ravinement surface formed over a landward and lateral migration of an estuary/bay mouth during transgression (Zaitlin et al., 1994; Nordfjord et al., 2006). However, no evidence of tidal scour has been identified at the upper boundary of S3a to corroborate the tidal origin of this ravinement surface. R2 has also been interpreted as a ravinement surface, without the ability to define the processes occurring during transgression (i.e. tidal or wave/shoreface ravinement).

Lithostratigraphy

Based on multiproxy analysis of the four piston cores, i.e. 003PC, 006PC, 008PC and 011PC, four lithological units were defined for the uppermost offshore sedimentary sequence in the northern–central part of the GSJ.

Unit L1

Unit L1 is present in the basal part of core 008PC below 240 cm (Fig. 7). It is composed of well-indurated grayish brown (base) to olive gray (top) clayey silt that is present as angular pebbles that were possibly crushed by piston coring and core handling. The upper boundary of unit L1 is characterized by a sharp contact, as well as 5 cm of mixed small angular pebbles and grayish brown gravelly muddy sand. A non-crushed section of unit L1 is also present in the last 13 cm of core 001PC (Fig. 6). The log(Ti/Ca) ratio shows the highest core values in unit L1 of core 008PC, with a radical decline in values prior to the erosional contact between L1 and L2b.

Based on the indurated configuration of the sediments coupled with the seismostratigraphic context of cores 008PC and 001PC, we suggest that unit L1 coincides with seismic unit S0 that was identified in this study as the seismic basement (Fig. S4). The high values of log(Ti/Ca) observed in L1 indicate a predominance of detrital components over biogenic carbonate, which could be interpreted as the control of sedimentation by fluvial inputs, enhanced coastal erosion of the inner gulf shores, relative sea-level rise or an increase in eolian supply (Tjallingii et al., 2010; Rothwell and Croudace, 2015, and references therein). Unit L1 could thus correspond to Miocene deposits related to marine–estuarine (Chenque Formation) or fluvial–subaerial depositional environments (Santa Cruz Formation; Nullo and Combina, 2002; Paredes, 2002).

Unit L2

The thickest (64 cm) and most detailed interval of unit L2 was observed in core 003PC (Fig. 7). In this core, unit L2 can be divided into two subunits: the lowermost unit L2a, from 396 to 363 cm, and the uppermost unit L2b, from 363 to 332 cm. Unit L2a is composed of an intercalation of light olive gray to grayish green medium silt and light gray/blue very-fine silt beds with thicknesses varying from 1 mm to ~1 cm. The median grain size ranges from 7.5 to 6 ϕ (Fig. 7). These wavy

structures are occasionally draped by very thin (~1 mm) dark gray silty sand beds (Fig. 8A). Unit L2a is thus characterized by small-scale heterolithic bedding with a multidirectional foreset pattern, which are interpreted as mud flasers coupled with rare and scarcely defined ripple foresets (medium silt). Between 378 and 374 cm, unit L2a is interlayered by lighter sediments, including a significant proportion of evaporite minerals (i.e., gypsum; Fig. 8A), as revealed by scanning electron micrographs and the geochemical composition of sediment samples retrieved from this layer (Fig. S3). Unit L2b is composed of finely laminated clayey silt with a noticeable transition in the main color from gray to olive gray at 353 cm. In unit L2b, the median grain size decreases with values oscillating at ~7 ϕ (Fig. 7). The configuration of unit L2b comprises millimeter-scale subparallel sedimentary rhythmites (Fig. 8B). The upper part of unit L2b shows soft-sediment deformation structures, defined by internally distorted and folded laminations with normal microfaults, bounded at the top by a scarcely defined contact coupled with an ~10-cm-thick shell-rich bed (Fig. 8B).

The boundary between subunits L2a and L2b is gradational, and the basal part of unit L2 was not recovered in core 003PC. The log(Ti/Al) ratio displays the lowest values in unit L2a and in the basal part of L2b, followed by a sharp increase in values in almost 20 cm of unit L2b, which coincides with the noticeable color transition of sediments starting at 353 cm (Fig. 7). A thinner section (~6 cm) of unit L2b with erosional upper and lower boundaries is also observed in core 008PC (Fig. 7).

The presence of heterolithic beds and sedimentary rhythmites in units L2a and L2b, with rhythmic variations in composition, color and grain size, indicates that these units were produced under regularly repeating changes in sediment supply and physical conditions of sedimentation (Fig. 8A and B; Reineck and Singh, 1980). The configuration and combined presence of these sedimentary structures suggest that units L2a and L2b were formed in tidally influenced depositional environments (e.g., Hovikoski et al., 2007; Reineck and Singh, 1980; Flemming, 2012). The sedimentary facies of unit L2a, with flaser structures in muddy sediments intercalated with coarser silty layers, as well as ripples of medium silt, resemble the facies of tidal flat sequences (Fig. 8A; Reineck and Singh, 1980).

Furthermore, the gypsum-rich layer in L2a indicates an environment favorable for evaporation, with shallow waters and possibly slight freshwater inputs. Such depositional environments have been previously described and interpreted as hypersaline lagoon/marsh deposits in Holocene stratigraphic reconstructions along the coast close to the GSJ (Bahía Camarones; Zanchetta et al., 2012). The interpretation of units L2a and L2b as deposits of lagoonal/wind–tidal flat environments under semi-arid conditions is also suggested based on the lack of fossils (i.e. bivalve shells and foraminifera), as well as the presence of light olive gray and grayish green clayey bedding (Reineck and Singh, 1980, and references therein). The slightly finer-grained and subparallel laminations of unit L2b indicate a gradational transition to lower-energy conditions (i.e. lower-velocity flows), as well as a possible decrease in tidal influences in the depositional processes. The sharp increase in the log(Ti/Ca) ratio at the level of the sediment color transition in unit L2b points toward an increase in Ti in sediments in comparison to Ca. The increased presence of Ti could be interpreted as a significant increase in terrigenous inputs during the deposition of this layer. Such a transition of conditions recorded in unit L2b could suggest an evolution of the depositional environment that was possibly related to sea-level rise with an increase in terrigenous fluxes from transgressive erosion and reworking on the shelf and/or inputs of material from southern Patagonian rivers (e.g., Tjallingii et al., 2010; Rothwell and Croudace, 2015; Li et al., 2019). With sea level hypothetically reaching the GSJ, a dominant northward-flowing current may have transported terrigenous sediment from larger rivers and the shelf to the north and thus to the gulf (Violante et al., 2014).

Units L3 and L4

The uppermost units, L3 and L4, are present in all cores (Fig. 7). Unit L3 consists of massive to crudely stratified light olive gray clayey silt with abundant and diffuse color mottles. The median grain size ranges from 8 to 7 ϕ (Fig. 7). The sediments are extensively bioturbated and contain numerous bivalve shells and shell fragments, including shell beds. In core 003PC, the base of unit L3 is characterized by a gradational boundary with unit L2, whereas in core 008PC, these units are divided by a sandy layer with lower and upper erosional boundaries, from 213 to 229 cm. This layer consists of very poorly sorted [sorting (ϕ) > 2] light gray sand with gravels, including some well-rounded very coarse pebbles.

Unit L4 is composed of olive gray silty clay with occasional bivalve shells and shell fragments. Compared to L3, the median grain size decreases slightly to reach values closer to 8 ϕ (Fig. 7). This extensively bioturbated unit shows mottled textures that are visible only in CT images. Its thickness varies from 175 cm in core 008PC to 375 cm in core 011PC. The boundary between units L3 and L4 is gradational and is coupled with a multi-centimeter-thick shell bed in cores 003PC and 011PC (Fig. 8C). However, the boundary between these two units is not clearly defined in core 008PC but could also be associated with a shell bed identified in this section of the core.

In units L3 and L4, the log(Ti/Ca) ratio displays a relatively common pattern in all cores, with slightly increasing values in unit L3, which are significantly accentuated close to the transition between L3 and L4, followed by constantly higher values in the upper parts of the latter unit. Magnetic susceptibility data depict progressively declining values in unit L3, as well as in the basal section of L4, and then constant lower values ($<50 \times 10^{-5}$ SI) in the upper parts of L4, except for the sandy layer observed between 213 and 229 cm in 008PC, which is characterized by an abrupt increase in magnetic susceptibility values ($>200 \times 10^{-5}$ SI).

The abundant bioturbation structures and massive silty clay to clayey silt in units L3 and L4 denote sediments deposited under marine conditions with low rates of sedimentation and deeper waters. The properties and configuration of L3 and L4 in cores 003PC, 006PC and 008PC suggest that these units correspond to the progressive development of inner-shelf hemipelagic deposits (Reineck and Singh, 1980, and references therein). The slightly and almost steady fining-upward evolution of grain size, especially in core 003PC, coupled with the increasing values of the log(Ti/Ca) ratio in units L3 and L4, are interpreted as representing the gradual evolution toward distal and lower-energy marine conditions related to sea-level variations. In the main and upper parts of L4, the relatively constant and stable physical and geochemical proxies also suggest the development and preservation of a marine depositional environment in the GSJ until the contemporary surface sediments at the core tops. Furthermore, the lower and almost constant to slightly increasing values of log(Ti/Ca) in L3 represent sedimentation that is more proximal to coastal conditions than L4, indicating an environment that was in transition between the coastal tidally influenced environment of L2 and the marine hemipelagic environment of L4 (Fig. 7).

In both cores 003PC and 008PC, the contact between L2b and L3 is sharp, which can be considered to indicate an abrupt event. The shell-rich bed at the base of L3 coupled with soft-sediment deformation structures at the top of L2b in 003PC and the coarse-grained deposits (including coarse sand and pebbles) at the top of L2b in 008PC suggest a wave ravinement surface sculpted by waves during coastline transgression (Swift, 1968; Zecchin et al., 2019, and references therein). In 003PC, both the preservation of underlying deposits L2a and L2b and the thin fine-grained transgressive lag point to a ravinement surface associated with low wave energy and rapid sea-level rise (Hwang and Heller, 2002; Zecchin et al., 2019). The lithological differences in the transgressive lags between 003PC and 008Pc may be explained by the geographical and/or topographic disparity between the two sites. The topographic gradient and bathymetry tend to influence the extent, depth and shape of the wave ravinement surface (Zecchin et al., 2019).

Chronology and sedimentation rates

The conventional and calibrated ages are reported in Table 2. To compare and discuss the chronostratigraphic records previously published for the GSJ area (Schellmann and Radtke, 2010), the radiocarbon ages from our study are presented using the median of the calibrated ages with a ΔR of 0 (see details in the radiocarbon dating section). In core 003PC, samples of isolated shell fragments or bivalve shells from the shell beds retrieved near the base of L3 yield ages between 13.8 and 13.6 cal ka BP. The homogeneous ages, with potentially overlapping ages in the order of their respective standard error (Table 2), in a section of almost 30 cm, suggest intense reworking of sediments that was possibly related to bioturbation, as well as extreme and abrupt events, such as storm waves, which is also supported by the concentrated fragments and complete shells in shell beds. Similar ages from 14 to 13.8 cal ka BP were also obtained in the basal part of light olive gray clayey silt (L3) in 006PC. Therefore, these ages collected at the base of L3 in 003CP, and coupled with the presence of a gradational contact between L2b and L3, suggest that the transition to inner shelf hemipelagic sedimentation occurred at ~14 cal ka BP in this part of the GSJ. The oldest age of 42 cal ka BP that was recovered at the transition between L2b and L3 in 008PC is consistent with the potential reworked origin of this deposit. With this in mind, the age–depth model and the related sedimentation rates of this section of 008PC are presented as a guide and are not considered in the rationale of this study.

The calculated sedimentation rates for the sedimentary sequence covered by the age–depth models range between 7 and 150 cm ka^{-1}. The highest sedimentation rate of 150 cm ka^{-1} has been found in cores 003PC and 006PC in the basal part of unit L3, which is characterized by several multi-centimeter-thick shell beds and potential severe reworking. Due to the homogeneous and potentially overlapping radiocarbon ages in this section, the sedimentation rates have been generated using the samples retrieved at the top and at the base of the sequence of interest (i.e. basal part of L3) in cores 003PC and 006PC. According to the age–depth model from 003PC, sedimentation rates decreased to 45 cm ka^{-1} at the top of L3. Furthermore, lower accumulation rates of 22 and 17 cm ka^{-1} have been calculated for the same sequence in cores 006PC and 011PC, respectively. Above the shell bed that marks the transition between L3 and L4, sedimentation rates decrease to the lowest values observed in the cores, with rates not exceeding 11 cm ka^{-1} during the early Holocene. The sedimentation rates then increase slightly to ~22 cm ka^{-1} in the mid- and late Holocene in cores 003PC and 008PC. For the same period, higher sedimentation rates of ~50 cm ka^{-1} have been calculated for the most distal core, 011PC.

Discussion

Incised valley development and infilling

The numerous infilled channels and valleys incising the Neogene–Paleogene deposits (i.e. uppermost Santa Cruz and Chenque Formations), which are observed mainly in the central part of the gulf (Figs. 3, 4 and 5a), confirm the existence of a paleo-fluvial network since the burial by sediment associated with marine transgressions (Violante et al., 2014). According to the ages of 11.4 and 12.7 cal ka BP obtained for sediment overlying the subaerial unconformity SB (001PC and 008PC, respectively; Figs. 6 and S4), incised channels and valleys developed during a pre-Holocene cycle of incision, primarily as a result of the erosional dynamics of rivers that are associated with sea-level fall (Zaitlin et al., 1994). The relatively widely spaced seismic grid (Fig. 1) collected during the expedition precludes the establishment of a paleodrainage pattern in the gulf. Nevertheless, several orientations of the incised valleys, essentially to the south and the southeast of the study area, can be observed in the seismic profiles and show that the channels were orientated toward the center of the GSJ and then directed offshore toward the shelf edge. However, we cannot confirm or refute the presence of a centripetal drainage pattern, as suggested by Violante et al. (2014).

Considering the large size of some incised valleys in the GSJ, the absence of seismic units showing fluvial deposits is noteworthy. However, the size of the drainage area of the rivers is also a predominant factor in explaining the thickness and the volume of valley-fill successions (Chaumillon et al., 2008). The absence of present-day major tributaries in the study area could suggest small rivers flowing into the gulf during lowstand periods followed by the absence of fluvial deposits in the valleys. Furthermore, a mesotidal to macrotidal regime is currently present in the GSJ, and similar conditions could have taken place during the transgressions, based on the shelf morphology in the area (Fig. 1a; Ponce et al., 2011). The strong tidal currents associated with the macrotidal regime could lead to the deep ravinement of underlying incised valley fill, including fluvial and/or transgressive deposits, as observed in modern sediment-starved estuarine/lagoonal systems along the French coasts (Chaumillon et al., 2010). In wave- and tide-dominated environments, the poorly developed lowstand systems tract can be entirely eroded by deep tidal ravinement surfaces (Féniès et al., 2010). The morphology of some broader valleys identified in the gulf may also result from cutting of the subaerial unconformity surface by energetic tidal currents (Fig. 4; e.g., Nordfjord et al., 2005; Scasso and Cuitiño, 2017).

In line with the interpretation of seismic units S1a, S1b, S2 and S3a, the incised valleys are characterized by transgressive infilling associated with central basin-like conditions in a mixed wave- and tide-dominated estuary. According to the geometry and architecture of the valley fill, we also suggest that the incised valley was filled during one lowstand–highstand sea-level cycle. However, the depth discordance of the upper surfaces of seismic units in the main incised valley (Units S1a and S1b) and other valleys (Units S2 and S3a) may indicate that some infilling of the main incised system occurred during a preceding sea-level cycle. Similar to the incised valleys described in the northern part of the ACS that are close to the Río de la Plata estuary, which are filled with post-LGM transgressive deposits (Violante et al., 2014,

and references therein), we propose that the central basin deposits filling the paleochannels in the GSJ, with the exception of the main incised valley, were deposited during the last marine transgression.

From marine incursions to present-day conditions in the GSJ

During the last glacial events, the ACS was exposed, forming an extensive subaerial plain (Rabassa et al., 2005). According to the sea-level curve for the ACS since the late Pleistocene proposed by Guilderson et al. (2000), the LGM lowstand was ~105 m below present sea level at ~18 ka (Fig. 10). The early stages of the post-LGM transgression are characterized by rapid sea-level rise, which could have led to the immersion of half of the emerged shelf plain at ~15.3 cal ka BP (Fig. 1a; Violante and Parker, 2004; Ponce et al., 2011; Violante et al., 2014). Ponce et al. (2011) proposed the onset of sea flooding in the GSJ related to the marine transgression, between 15 and 15.5 cal ka BP, when sea level reached −90 m. This chronology could not be confirmed with the radiocarbon ages obtained in the sediment cores from the central part of the gulf used in our study (Figs. 9 and 10). Nevertheless, we propose that the onset of hydrodynamic conditions favorable for inner shelf subtidal sedimentation occurred at ~14 cal ka BP in accordance with ages collected at the base of unit L3 in cores 003PC and 006PC.

Prior to 14 cal ka BP, the transition between the central basin estuarine environment (units S2 and S3a) and shallow water depositional environments (L2a and L2b), marked by a ravinement surface, advocates for migration of the shoreline adjacent to the gulf. The lithological interpretation of units L2a and L2b at the base of 003PC suggests the presence of lagoonal/wind–tidal flat environments during this period, with a progressive evolution to a subtidal environment as a result of sea-level rise. The development of lagoonal/wind–tidal conditions in the gulf may have been promoted by sand bodies (unit S3) that form a shallow NNE-facing bank dividing the southern half of the GSJ from the shelf (Figs. 1b and 5b). This configuration, with an estuary mouth that is partially closed by sand bodies/spits leading to the development of a lagoonal environment, shows some similarities to the present-day 'Arcachon Basin', in which the Leyre estuary was transformed into a lagoon during the late Holocene (Allard et al., 2009; Féniès et al., 2010). The sand bank could have been formed during the last marine transgression or previous transgressive/highstand cycles, notably with the transport of coarse material from the Deseado River by a strong longshore current.

From ~14 cal ka BP and the beginning of the dominance of subtidal sedimentation, the depositional environment in the central part of the GSJ presented progressive development toward distal and lower energetic oceanic conditions, which led to the onset of actual marine sedimentation in the gulf. According to the lithological interpretation of L3 and L4 coupled with the log(Ti/Ca) ratio, a shallow subtidal environment was maintained from ~14 to ~11.5 cal ka BP, followed by a distinct evolution to a marine hemipelagic environment prior to ~7 cal ka BP (Fig. 10). Thus, we confirmed the appearance of

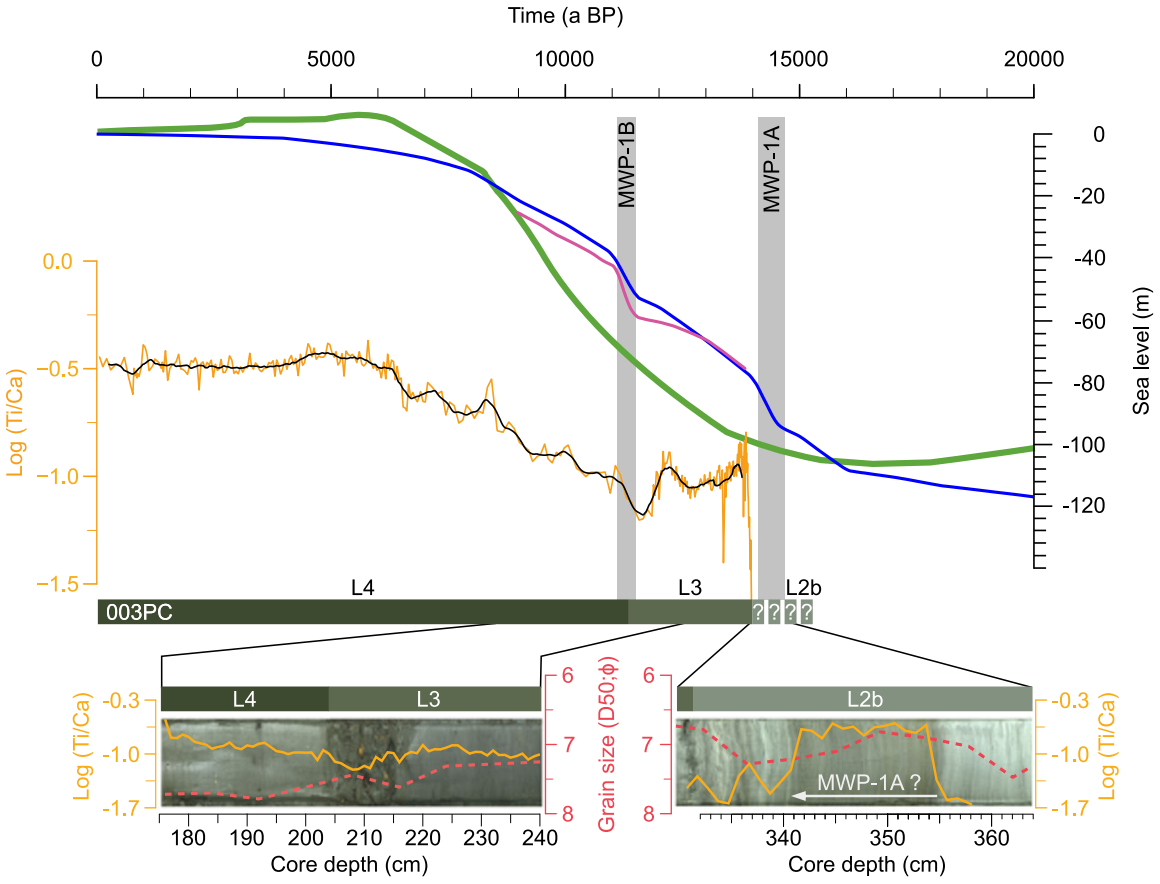

Figure 10. Comparison between the log(Ti/Ca) ratio values of core 003PC (red curve) and the eustatic and relative sea-level curves since 20 ka BP. A 400-year running mean of log(Ti/Ca) raw values is also presented (black curve). Selected intervals of log(Ti/Ca) ratios (yellow curve) and median grain size (red dotted curve; ϕ) are superimposed over respective sections in core photographs. The eustatic sea-level curves were generated from the prediction of the sea-level history using the ICE-5G model (blue curve; Peltier and Fairbanks, 2006), as well as a reconstruction from the Barbados coral reefs (purple curve; Abdul et al., 2016) and adapted from Jakobsson et al. (2017). The estimated time intervals of MWP-1A and MWP-1B are presented with gray columns. The relative sea-level curve for the ACS (green curve) was compiled by Violante and Parker (2004) after Cavallotto et al. (1995) and Guilderson et al. (2000). [Color figure can be viewed at wileyonlinelibrary.com]

inner-shelf environments in the central part of the gulf during the Holocene, as suggested by Boltovskoy (1954). However, this part of the GSJ seems to expose no lithological or physical evidence of Holocene sea-level changes observed in beach ridges and littoral terraces of the gulf area (e.g., Schellmann and Radtke, 2010, and references therein; Zanchetta et al., 2012; 2014). Nevertheless, the lithological transition between L2b and L3 in 003PC and to a lesser extent between L3 and L4 in every piston core except 001PC signifies the evolution of sedimentary environments related to sea-level rise prior to the Holocene.

The radiocarbon ages of ~14 cal ka BP and the wave ravinement surface obtained at the base of L3 suggest that the transition between this unit and L2b could be consistent with an abrupt sea-level rise event (~20 m; Harrison et al., 2019), with an estimated age between 14.6 and 13.6 cal ka BP (records from Barbados and Tahiti; Fairbanks, 1989; Bard et al., 1996; Peltier and Fairbanks, 2006; Deschamps et al., 2012; Fig. 10). This abrupt and global sea-level jump is associated with a brief and high-amplitude glacial discharge (deglacial meltwater pulse: MWP-1A; Fairbanks, 1989). In the second part of L2b, the abrupt increase in the log(Ti/Ca) ratio in a distinct multi-centimeter-thick layer seems to indicate that the rapid sea-level change could have started prior to 14 cal ka BP in the GSJ, before the transition between L2b and L3 (Figs. 7 and 10). Substantial inputs of terrigenous sediment in the gulf could support the beginning of this rapid jump in base level and the wave ravinement surface related to this rapid flooding of the deep central part of the GSJ. Furthermore, the abrupt sea-level rise event may have been preceded by a phase of stillstand, as suggested by the aggrading/normal regressive phase of tidal flat/lagoonal deposition observed in cores 003PC and 008PC (L2a and L2b). Evidence suggesting the effects of MWP-1A, which occurred between 14.6 and 14 cal ka BP, on the ACS have been previously highlighted by the sea-level curve proposed by Guilderson et al. (2000).

The relative sea-level curve for the ACS also presents a record of an analogous event at ~11.5 cal ka BP that is consistent with MWP-1B (Fairbanks, 1989; Bard et al., 1996; Guilderson et al., 2000; Abdul et al., 2016; Fig. 10). Unfortunately, the relative sea-level curve generated by Violante and Parker (2004), compiled after the results of Guilderson et al. (2000) and Cavallotto et al. (1995) and presented in this article, does not have sufficient resolution to highlight MWP-1A and MWP-1B (Figs. 2 and 10). Isla et al. (2013) suggest that the San Matías Gulf, located ~350 km north of the GSJ and characterized by a sill at a depth of 60 m, should have been flooded during MWP-1B. In the GSJ, the slight transition of depositional conditions separating L3 and L4 and estimated to between 11.9 and 11.6 cal ka BP (records from a shell-rich bed; 11.1 cal ka BP in 006PC) could be correlated to the sea-level jump related to MWP-1B. However, the slight and constant increase in the log(Ti/Ca) ratio and grain size does not seem consistent with a distinct change in the elemental composition and morphological characteristics of sediments (Figs. 7 and 10). Indeed, if the depositional environment presents a progressive transition to the onset of marine hemipelagic conditions from ~11.5 cal ka BP in this part of the gulf, it appears highly speculative to suggest that clear evidence of MWP-1B is present in our sedimentary records. Furthermore, the existence and intensity of MWP-1B, as dated between 11.1 and 11.5 cal ka BP (records from Barbados and Tahiti; Fairbanks, 1989; Bard et al., 1996; Abdul et al., 2016), remains controversial and is disputed (e.g., Lambeck et al., 2014; Bard et al., 2016; Harrison et al., 2019).

According to age–depth models, the sedimentation rates during the Holocene appear to be relatively low, with values ranging between 7 and 23 cm ka^{-1}, in comparison to other gulfs with similar morphological and environmental conditions for which the deposition rates frequently exceed 100 cm ka^{-1} during the same period (e.g. Gulf of Cadiz, Spain; Nelson et al., 1999). The main difference between those gulfs and the GSJ is the absence of any present-day major and perennial tributaries in our area of interest, which are likely to have significantly affected the terrigenous inputs. The continuation of these sedimentation rates throughout the Holocene in the central part of the gulf suggests that the impact of riverine inputs on sedimentary processes and the origins of terrigenous sediments during this period could be relatively close to modern ones. Moreover, the progressive diminution and withdrawal of the eastern flank of the Northern Patagonian Icefield through the Deseado River during the early and mid-Holocene, which could have been a potential large source of terrigenous inputs for the GSJ, could not be highlighted by the sedimentation rates and the lithological interpretation of the sediment cores. Since the first Atlantic to Pacific drainage reversal event, which occurred at ~15.3 cal ka BP (Thorndycraft et al., 2019), 12.8 cal ka BP (Turner et al., 2005) or 10.5 ka BP (Glasser et al., 2016), and especially since the capture of the Deseado River meltwater drainage by the Baker River watershed flowing into the Pacific Ocean (Fig. 1a), the discharge of the Deseado River has drastically decreased, with potential effects on sedimentation in the GSJ (Isla et al., 2013). However, the increase in log(Ti/Ca) ratios from the early Holocene displays an opposite trend to the potential diminution of fluvio-glacial outflows through the Atlantic coast, which is consistent with the eustatic and relative sea-level curves (Fig. 10). These results illustrate the dominant contribution of sea-level rise to the log(Ti/Ca) ratio and thus to the terrigenous clastic inputs in the GSJ during the early to mid-Holocene. The results also support the notion that as the sea level rose to its near-modern position over this period, external/oceanic inputs, coastal erosion of the inner gulf shores and the eolian transport all drove the detrital input and the sediment dynamics within the GSJ (Desiage et al., 2018). Finally, the higher sedimentation rate since the mid-Holocene observed in the most external core (i.e. ~50 cm ka^{-1}; 011PC) seems to confirm a leading role of external/oceanic contributions to these sedimentary inputs (Desiage et al., 2018).

Conclusions

After the analysis of hundreds of kilometers of high-resolution geophysical profiles, as well as five piston cores, the first detailed description of the upper sedimentary sequence of the late Quaternary deposits in the GSJ is presented. Five seismic facies have been defined, including the acoustic basement whose surface presents incised erosional truncation that formed valleys and channels. These numerous infilled channels and valleys confirmed the existence, in this sector of the ACS, of a paleo-fluvial network that was buried by central basin estuarine deposits during the last marine transgression.

Lithostratigraphic investigation of the post-LGM depositional sequence in the gulf, as illustrated by seismic unit S4, has favored the identification and description of four sedimentary units and subunits. According to the lithologic and chronostratigraphic interpretation of sedimentary records, we suggest that the onset of subtidal sedimentation occurred at ~14 cal ka BP in this part of the gulf. The evolution of hydrodynamic conditions favorable to these depositional environments could have been facilitated by an abrupt sea-level rise related to MWP-1A that was possibly identified in

unit L2b, as reported by the identification of a wave ravinement surface and log(Ti/Ca) ratios. Interpretation of lagoon/tidal flat deposit units L2a and L2b may suggest a stillstand phase prior to MWP-1A. Overall, this study highlights the significant impact of sea-level rise on sedimentation in the gulf from the onset of marine invasion to the mid-Holocene, and the reduced contribution, as currently observed, of riverine inputs due to the progressive diminution and withdrawal of glacial drainage starting before the Holocene. Finally, the results presented in this paper confirm the beginning of sea flooding related to the last marine transgression prior to 14 cal ka BP, as well as the establishment of modern sedimentary conditions during the mid-Holocene.

Acknowledgments. We acknowledge the comprehensive editorial approach of Nicholas Balascio, as well as the constructive and helpful reviews of Andrew Green and an anonymous reviewer, which helped to significantly improve the paper. The authors sincerely thank the captain, crew and scientific participants of the COR1404 (MARES and MARGES) expedition on board the R/V *Coriolis II*. Financial support for MARES and MARGES expeditions was provided by the Ministerio de Ciencia, Tecnología e Innovación Productiva (MINCyT), Provincia de Chubut and Consejo Nacional de Investigaciones Científicas y Técnicas (CONICET). This research was funded by the Natural Sciences and Engineering Research Council of Canada (NSERC) through Discovery grants to G. St-Onge and J.-C. Montero-Serrano and by the Fonds de recherche du Québec – Nature et Technologies (FRQNT) through a team grant to G. St-Onge, J.-C. Montero-Serrano and A. Rochon. The use of VISTA Desktop Seismic Data Processing and Kingdom Suite® software was made possible by Schlumberger and IHS Inc., respectively, through university partnership programs. We are grateful to Quentin Beauvais for technical support.

Author contributions—Pierre-Arnaud Desiage: Conceptualization (Lead); Formal analysis (Lead); Methodology (Lead); Writing – original draft (Lead). Guillaume St-Onge: Conceptualization (Supporting); Funding acquisition (Lead); Project administration (Lead); Resources (Lead); Supervision (Equal); Writing – review & editing (Supporting). Mathieu J. Duchesne: Formal analysis (Supporting); Methodology (Supporting); Supervision (Equal); Writing – review & editing (Supporting). Jean-Carlos Montero-Serrano: Conceptualization (Supporting); Formal analysis (Supporting); Funding acquisition (Supporting); Methodology (Supporting); Project administration (Supporting); Resources (Supporting); Supervision (Equal); Writing – review & editing (Supporting). Miguel J. Haller: Funding acquisition (Supporting); Writing – review & editing (Supporting).

Data availability statement

The chronological, geophysical and geochemical data that support the findings of this study are openly available in Pangaea. https://doi.org/10.1594/PANGAEA.941235

The geophysical data that support the findings of this study are available on request from the corresponding author.

Supporting information

Additional supporting information can be found in the online version of this article.

Figure S1. Correlation between piston (PC) and box cores (BC) using *a** for cores 003PC and 011PC, and relative content of Fe for cores 006PC and 008PC. To compensate for the absence of a box core for 003PC, this core was correlated with the closest 'depth-corrected' piston core (011PC). Properties for the PC and BC are presented in black and orange, respectively, except in the case of 003PC in which 011PC is shown in orange.

Figure S2. Biplot of PC1 versus PC2 generated from the log-centered transformation of pXRF data. Statistical calculations were conducted with R software using the packages 'compositions' (van den Boogaart and Tolosana-Delgado, 2008) and 'vegan' (Oksanen et al., 2019). Prior to all multivariate analyses, a log-centered (clr) transform was applied to the data (Aitchison, 1990).

Figure S3. Scanning electron microscopy (SEM) images of the bulk fraction of sediment samples retrieved from the potential gypsum-rich layer at 376 cm in 003PC. Elemental composition (wt%) of five particles (10 spectra) is tabulated below.

Figure S4. Interpreted high-resolution sparker seismic profiles (section of lines 004bis, 012bis and 014; A, B and C) showing the locations of cores 001PC, 006PC and 008PC, respectively.

Abbreviations. ACS, Argentine Continental Shelf; BC, box core; BP, before present (1950 calendar year); GC, gravity core; GSJ, Gulf of San Jorge; LGM, Last Glacial Maximum; MSCL, multi-sensor core logger; MWP, meltwater pulse; PC, piston core; SEM, scanning electron microscope; XRF, X-ray fluorescence.

References

Abdul, N.A., Mortlock, R.A., Wright, J.D. & Fairbanks, R.G. (2016) Younger Dryas sea level and meltwater pulse 1B recorded in Barbados reef crest coral Acropora palmata. *Paleoceanography*, 31, 330–344.

Aitchison, J. (1990) Relative variation diagrams for describing patterns of compositional variability. *Math. Geol.* 22, 487–511.

Allard, J., Chaumillon, E. & Féniès, H. (2009) A synthesis of morphological evolutions and Holocene stratigraphy of a wave-dominated estuary: The Arcachon lagoon, SW France. *Cont. Shelf Res.* 29, 957–969.

Allen, G.P. & Posamentier, H.W. (1994) Transgressive facies and sequence architecture in mixed tide and wave-dominated incised valleys: example from the Gironde estuary, France. In: Dalrymple, R.W., Boyd, R. & Zaitlin, B.A. (Eds.) *Incised Valley Systems: Origin and Sedimentary Sequences*, 51. Society of Economic Palaeontologists and Mineralogists Special Publication. pp. 226–240.

Bard, E., Hamelin, B., Arnold, M., Montaggioni, L., Cabioch, G., Faure, G. et al. (1996) Deglacial sea-level record from Tahiti corals and the timing of global meltwater discharge. *Nature*, 382, 241–244.

Bard, E., Hamelin, B., Deschamps, P. & Camoin, G. (2016) Comment on "Younger Dryas sea level and meltwater pulse 1B recorded in Barbados reefal crest coral Acropora palmata" by NA Abdul et al. *Paleoceanography*, 31, 1603–1608.

Barnhardt, W.A., Roland Gehrels, W. & Kelley, J.T. (1995) Late Quaternary relative sea-level change in the western Gulf of Maine: Evidence for a migrating glacial forebulge. *Geology*, 23, 317–320.

Bellosi, E. (1990). Formación Chenque: Registro de la transgresión patagoniana (Terciario medio) de la cuenca de San Jorge, Argentina, in: Actas 11 Congreso Geológico Argentino, San Juan. pp. 57–60.

Bernallack, K., Green, A.N., Humphries, M.S., Cooper, J.A.G., Dladla, N.N. & Finch, J.M. (2016) The stratigraphic evolution of a large back-barrier lagoon system with a non migrating barrier. *Marine Geology*, 379, 64–77.

Bini, M., Zanchetta, G., Ribolini, A., Salvatore, M.C., Baroni, C., Pappalardo, M. et al. (2017) Last Interglacial Sea-level highstand deduced from notches and inner margins of marine terraces at Puerto Deseado, Santa Cruz Province, Argentina. *Geogr. Fis. e Din. Quat.* 40, 29–39.

Blaauw, M. & Christen, J.A. (2011) Flexible paleoclimate age-depth models using an autoregressive gamma process. *Bayesian analysis (Online)*, 6, 457–474.

Blanchet, C.L., Thouveny, N. & Vidal, L. (2009) Formation and preservation of greigite (Fe3S4) in sediments from the Santa Barbara Basin: Implications for paleoenvironmental changes during the past 35 ka. *Paleoceanogr. Paleoclimatology*, 24, PA2224.

Blott, S.J. & Pye, K. (2001) GRADISTAT: a grain size distribution and statistics package for the analysis of unconsolidated sediments. *Earth Surf. Process. Landforms*, 26, 1237–1248.

Boltovskoy, E. (1954) Foraminíferos del Golfo San Jorge. Revista del Instituto Nacional de Investigaciones y Museo Argentino de Ciencias Naturales 'Bernardino Rivadavia'. *Ciencias Geológicas*, 3, 85–246.

Cavallotto, J.L., Parker, G. & Violante, R.A. (1995) Relative sea level changes in the Río de la Plata during the Holocene. In: 2 Annual Meeting of International Geoscience Programme 367: Late Quaternary Coastal Records of Rapid Change: Application to Present and Future Conditions. pp. 19–20.

Cavallotto, J.L., Violante, R.A. & Parker, G. (2004) Sea-level fluctuations during the last 8600 years in the de la Plata River (Argentina). *Quat. Int.* 114, 155–165.

Chaumillon, E., Proust, J.-N., Menier, D. & Weber, N. (2008) Incised-valley morphologies and sedimentary-fills within the inner shelf of the Bay of Biscay (France): a synthesis. *J. Mar. Syst.* 72, 383–396.

Chaumillon, E., Tessier, B. & Reynaud, J.Y. (2010) Stratigraphic records and variability of incised valleys and estuaries along French coasts. *Bull. Soc. Géol*, 181, 75–85.

Chivas, A.R., García, A., van der Kaars, S., Couapel, M.J.J., Holt, S., Reeves, J.M. et al. (2001) Sea-level and environmental changes since the last interglacial in the Gulf of Carpentaria, Australia: an overview. *Quat. Int.* 83, 19–46.

Cordero, R.R., Panarello, H., Lanzelotti, S. & Dubois, C.M.F. (2003) Radiocarbon age offsets between living organisms from the marine and continental reservoir in coastal localities of Patagonia (Argentina). *Radiocarbon*, 45, 9–15.

Crockett, J.S. & Nittrouer, C.A. (2004) The sandy inner shelf as a repository for muddy sediment: an example from Northern California. *Cont. Shelf Res.* 24, 55–73.

Croudace, I.W. & Rothwell, R.G. (2015). Micro-XRF Studies of Sediment Cores: Applications of a non-destructive tool for the environmental sciences. Developments in Paleoenvironmental Research 17. Springer Netherlands, Dordrecht, 656 pp.

Deschamps, P., Durand, N., Bard, E., Hamelin, B., Camoin, G., Thomas, A.L. et al. (2012) Ice-sheet collapse and sea-level rise at the Bølling warming 14,600 years ago. *Nature*, 483, 559–564.

Desiage, P.-A., Montero-Serrano, J.-C., St-Onge, G., Crespi-Abril, A.C., Giarratano, E., Gil, M.N. et al. (2018) Quantifying sources and transport pathways of surface sediments in the Gulf of San Jorge, central Patagonia (Argentina). *Oceanography*, 31, 92–103.

Dladla, N.N., Green, A.N., Cooper, J.A.G. & Humphries, M.S. (2019) Geological inheritance and its role in the geomorphological and sedimentological evolution of bedrock-hosted incised valleys, lake St Lucia, South Africa. *Estuar. Coast. Shelf Sci.* 222, 154–167.

Duchesne, M.J. & Bellefleur, G. (2007). Processing of single-channel high-resolution seismic data collected in the St. Lawrence Estuary. Current Research of the Geological Survey of Canada 2007-D1, 11pp.

Duchesne, M.J., Bellefleur, G., Galbraith, M., Kolesar, R. & Kuzmiski, R. (2007) Strategies for waveform processing in sparker data. *Mar. Geophys. Res.* 28, 153–164.

Dyer, K.R. & Huntley, D.A. (1999) The origin, classification and modelling of sand banks and ridges. *Cont. Shelf Res.* 19, 1285–1330.

Fairbanks, R.G. (1989) A 17,000-year glacio-eustatic sea level record: influence of glacial melting rates on the Younger Dryas event and deep-ocean circulation. *Nature*, 342, 637–642.

Féniès, H., Lericolais, G. & Posamentier, H.W. (2010) Comparison of wave-and tide-dominated incised valleys: specific processes controlling systems tract architecture and reservoir geometry. *Bull. Soc. Géol. Fr*, 2, 171–181.

Figari, E.G., Strelkov, E., Laffitte, G., Cid de La Paz, M.S., Courtade, S.F., Celaya, J. et al. (1999) Los sistemas petroleros de la Cuenca del Golfo San Jorge: Síntesis estructural, estratigráfica y geoquímica, in: 4 Congreso de Exploración y Desarrollo de Hidrocarburos. pp. 197–237.

Fleming, K., Johnston, P., Zwartz, D., Yokoyama, Y., Lambeck, K. & Chappell, J. (1998) Refining the eustatic sea-level curve since the Last Glacial Maximum using far-and intermediate-field sites. *Earth and Planetary Science Letters*, 163, 327–342.

Flemming, B.W. (2012) Siliciclastic back-barrier tidal flats, In: *Principles of Tidal Sedimentology*. Springer. pp. 231–267.

Galloway, W.E. (1989) Genetic stratigraphic sequences in basin analysis I: architecture and genesis of flooding-surface bounded depositional units. *AAPG Bulletin*, 73, 125–142.

Glasser, N.F., Jansson, K.N., Duller, G.A., Singarayer, J., Holloway, M. & Harrison, S. (2016) Glacial lake drainage in Patagonia (13-8 kyr) and response of the adjacent Pacific Ocean. *Scientific Reports*, 6, 1–7.

Glorioso, P.D. & Flather, R.A. (1995) A barotropic model of the currents off SE South America. *Journal of Geophysical Research*, 100, 13427–13440.

Gómez, E.A., Borel, C.M., Aguirre, M.L. & Martínez, D.E. (2008) Radiocarbon reservoir ages and hardwater effect for the northeastern coastal waters of Argentina. *Radiocarbon*, 50, 119–129.

Green, A.N. (2009) Palaeo-drainage, incised valley fills and transgressive systems tract sedimentation of the northern KwaZulu-Natal continental shelf, South Africa, SW Indian Ocean. *Marine Geology*, 263, 46–63.

Green, A.N., Dladla, N.N. & Garlick, G.L. (2013) Spatial and temporal variations in incised valley systems from the Durban continental shelf, KwaZulu-Natal, South Africa. *Marine Geology*, 335, 148–161.

Guilderson, T.P., Burckle, L., Hemming, S. & Peltier, W.R. (2000) Late Pleistocene sea level variations derived from the Argentine Shelf. Geochemistry, Geophys. Geosystems 1.

Harrison, S., Smith, D.E. & Glasser, N.F. (2019) Late Quaternary meltwater pulses and sea level change. *J. Quat. Sci*, 34(1), 1–15.

Hovikoski, J., Gingras, M., Räsänen, M., Rebata, L.A., Guerrero, J., Ranzi, A. et al. (2007) The nature of Miocene Amazonian epicontinental embayment: High-frequency shifts of the low-gradient coastline. *Geological Society of America Bulletin*, 119, 1506–1520.

Hwang, I.-G. & Heller, P.L. (2002) Anatomy of a transgressive lag: Panther Tongue Sandstone, Star Point Formation, central Utah. *Sedimentology*, 49, 977–999.

Isla, F.I. (2013) The flooding of the San Matías Gulf: The Northern Patagonia sea-level curve. *Geomorphology*, 203, 60–65.

Isla, F.I., Espinosa, M. & Iantanos, N. (2015) Evolution of the Eastern flank of the North Patagonian Ice Field: The deactivation of the Deseado River (Argentina) and the activation of the Baker River (Chile). *Zeitschrift für Geomorphol*, 59, 119–131.

Isla, F.I., Iantanos, N. & Estrada, E. (2002) Playas reflectivas y disipativas macromareales del Golfo San Jorge, Chubut. *Rev. la Asoc. Argentina Sedimentol.* 9, 155–164.

Isla, F.I., Bujalesky, G.G., Bértola, G.R., Iantanos, N. & Estrada, E. (2006) Typology of Argentine beaches: composition, tidal range and wave energy. *J. Coast Res*, 39, 375–378.

Jakobsson, M., Pearce, C., Cronin, T.M., Backman, J., Anderson, L.G., Barrientos, N. et al. (2017) Post-glacial flooding of the Bering Land Bridge dated to 11 cal ka BP based on new geophysical and sediment records. *Clim. Past*, 13, 991–1005.

Kokot, R.R. (2004) Erosión en la costa patagónica por cambio climático. Rev. la Asoc. *Geológica Argentina*, 59, 715–726.

Kostadinoff, J. (1992) Estudio geofísico de la Península de Valdés y los golfos nordpatagónicos. *Rev. la Asoc. Geológica Argentina*, 47, 229–236.

Lambeck, K., Rouby, H., Purcell, A., Sun, Y. & Sambridge, M. (2014) Sea level and global ice volumes from the Last Glacial Maximum to the Holocene. *Proc. Natl. Acad. Sci.* 111, 15296–15303.

Liao, H.-R., Yu, H.-S. & Su, C.-C. (2008) Morphology and sedimentation of sand bodies in the tidal shelf sea of eastern Taiwan Strait. *Marine Geology*, 248, 161–178.

Martínez, O.A. & Kutschker, A. (2011) The 'Rodados Patagónicos'(-Patagonian shingle formation) of eastern Patagonia: environmental conditions of gravel sedimentation. *Biological Journal of the Linnean Society*, 103, 336–345.

Matano, R.P. & Palma, E.D. (2018) Seasonal variability of the oceanic circulation in the Gulf of San Jorge, Argentina. *Oceanography*, 31, 16–24.

McCave, I.N. (1972) Transport and escape of fine-grained sediment from shelf areas. Shelf sediment Transp. *Process pattern*, 225–248.

Menier, D., Reynaud, J.-Y., Proust, J.-N., Guillocheau, F., Guennoc, P., Bonnet, S. et al. (2006) Basement control on shaping and infilling of valleys incised at the southern coast of Brittany, France. SEPM Spec. Pub., Incised Valleys in time and space.

Milne, G.A., Long, A.J. & Bassett, S.E. (2005) Modelling Holocene relative sea-level observations from the Caribbean and South America. *Quaternary Science Reviews*, 24, 1183–1202.

Mitchum Jr., R.M., Vail, P.R. & Sangree, J.B. (1977) Seismic stratigraphy and global changes of sea level, part 6: stratigraphic interpretation of seismic reflection patterns in depositional sequences. In: Payton, C.E. (Ed.), *Seismic Stratigraphy - Applications to Hydrocarbon Exploration*. AAPG Memoir 26 pp. 117–133.

Mosher, D.C. & Simpkin, P.G. (1999) Environmental marine Geoscience 1. Status and trends of marine high-resolution seismic reflection profiling: Data acquistion. *Geosci. Canada*, 26, 174–188.

Mouzo, F.H. (2017) Geología submarina del golfo norpatagónico San Matías. *Rev. la Asoc. Geológica Argentina*, 74, 553–569.

Nelson, C.H., Baraza, J., Maldonado, A., Rodero, J., Escutia, C., Barber Jr. J.H. (1999) Influence of the Atlantic inflow and Mediterranean outflow currents on Late Quaternary sedimentary facies of the Gulf of Cadiz continental margin. *Marine Geology*, 155, 99–129.

Nittrouer, C.A. & Sternberg, R.W. (1981) The formation of sedimentary strata in an allochthonous shelf environment: the Washington continental shelf. *Marine Geology*, 42, 201–232.

Nordfjord, S., Goff, J.A., Austin Jr., J.A. & Sommerfield, C.K. (2005) Seismic geomorphology of buried channel systems on the New Jersey outer shelf: assessing past environmental conditions. *Marine Geology*, 214, 339–364.

Nordfjord, S., Goff, J.A., Austin Jr., J.A. & Gulick, S.P.S. (2006) Seismic facies of incised-valley fills, New Jersey continental shelf: implications for erosion and preservation processes acting during latest Pleistocene–holocene transgression. *J. Sediment. Res.* 76, 1284–1303.

Nullo, F.E. & Combina, A.M., (2002) Sedimentitas terciarias continentales, in: Congreso Geológico Argentino. pp. 245–258.

Ó Cofaigh, C., Weilbach, K., Lloyd, J.M., Benetti, S., Callard, S.L., Purcell, C. et al. (2019) Early deglaciation of the British-Irish Ice Sheet on the Atlantic shelf northwest of Ireland driven by glacioisostatic depression and high relative sea level. *Quatenary Science Reviews*, 208, 76–96.

Oksanen, J., Blanchet, F.G., Kindt, R., Legendre, P., Minchin, P.R., O'Hara, R.B. et al. (2019) vegan: Community Ecology Package (version 2.5-6).

Palma, E.D., Matano, R.P. & Piola, A.R. (2008) A numerical study of the Southwestern Atlantic Shelf circulation: Stratified ocean response to local and offshore forcing. *J. Geophys. Res. Ocean*, 113(C11).

Palma, E.D., Matano, R.P., Tonini, M.H., Martos, P. & Combes, V. (2020) Dynamical analysis of the oceanic circulation in the Gulf of San Jorge. *Argentina. J. Mar. Syst.* 113, 103261.

Panella, S., Michelato, A., Perdicaro, R., Magazzú, G., Decembrini, F. & Scarazzato, P. (1991) A preliminary contribution to the understanding of the hydrological characteristics of the Strait of Magellan: Austral spring 1989. *Bolletino Oceanol. Teor. Appl.* 9, 107.

Paredes, J.M. (2002) Asociaciones de facies y correlación de las sedimentitas de la Formación Chenque (Oligoceno-Mioceno) en los alrededores de Comodoro Rivadavia, Cuenca del Golfo San Jorge, Argentina. *Rev. la Asoc. Argentina Sedimentol.* 9, 53–64.

Parker, G., Violante, R.A. & Paterlini, M.C. (1996) Fisiografía de la Plataforma Continental. In: Ramos, V. and Turic, M., Geología y Recursos Naturales de la Plataforma Continental Argentina. Relatorio XIII Congreso Geológico Argentino. Asociación Geológica Argentina, Buenos Aires, 1–16.

Parker, G., Paterlini, M.C. & Violante, R. (1997) El fondo marino.

Peltier, W.R. & Fairbanks, R.G. (2006) Global glacial ice volume and Last Glacial Maximum duration from an extended Barbados sea level record. *Quatenary Science Reviews*, 25, 3322–3337.

Perissoratis, C., Piper, D.J.W. & Lykousis, V. (2000) Alternating marine and lacustrine sedimentation during late Quaternary in the Gulf of Corinth rift basin, central Greece. *Marine Geology*, 167, 391–411.

Ponce, J.F., Rabassa, J., Coronato, A. & Borromei, A.N.A. (2011) Palaeogeographical evolution of the Atlantic coast of Pampa and Patagonia from the last glacial maximum to the Middle Holocene. *Biological Journal of the Linnean Society*, 103, 363–379.

Rabassa, J. (2008) Late cenozoic glaciations in Patagonia and Tierra del Fuego. *Dev. Quat. Sci*, 11, 151–204.

Rabassa, J., Coronato, A.M. & Salemme, M. (2005) Chronology of the Late Cenozoic Patagonian glaciations and their correlation with biostratigraphic units of the Pampean region (Argentina). *J. South Am. Earth Sci*, 20, 81–103.

Reimer, P.J., Bard, E., Bayliss, A., Beck, J.W., Blackwell, P.G., Ramsey, C.B. et al. (2013) IntCal13 and Marine13 radiocarbon age calibration curves 0–50,000 years cal BP. *Radiocarbon*, 55, 1869–1887.

Reineck, H.-E. & Singh, I.B. (1980) *Depositional sedimentary environments: with reference to terrigenous clastics*. Berlin-Heidelberg-New York: Springer-Verlag. p. 549.

Rostami, K., Peltier, W.R. & Mangini, A. (2000) Quaternary marine terraces, sea-level changes and uplift history of Patagonia, Argentina: comparisons with predictions of the ICE-4G (VM2) model of the global process of glacial isostatic adjustment. *Quatenary Science Reviews*, 19, 1495–1525.

Sangree, J.B. & Widmier, J.M. (1979) Interpretation of depositional facies from seismic data. *Geophysics*, 44, 131–160.

Scasso, R.A. & Cuitiño, J.I. (2017) Sequential development of tidal ravinement surfaces in macro- to hypertidal estuaries with high volcaniclastic input: the Miocene Puerto Madryn Formation (Patagonia, Argentina). *Geo-Mar Lett*, 37, 427–440.

Schellmann, G. & Radtke, U. (2010) Timing and magnitude of Holocene sea-level changes along the middle and south Patagonian Atlantic coast derived from beach ridge systems, littoral terraces and valley-mouth terraces. *Earth-Science Rev*, 103, 1–30.

Stuiver, M. & Reimer, P.J. (1993) Extended 14 C data base and revised CALIB 3.0 14 C age calibration program. *Radiocarbon*, 35, 215–230.

Svendsen, J.I., Elverhmi, A. & Mangerud, J. (1997) The retreat of the Barents Sea Ice Sheet on the western Svalbard margin. *Boreas*, 25, 244–256.

Swift, D.J. (1968) Coastal erosion and transgressive stratigraphy. *The Journal of Geology*, 76, 444–456.

Sylwan, C.A. (2001) Geology of the Golfo San Jorge Basin, Argentina. Geología de la Cuenca del Golfo San Jorge, Argentina. *J. Iber. Geol.* 27, 123–158.

Thorndycraft, V.R., Bendle, J.M., Benito, G., Davies, B.J., Sancho, C., Palmer, A.P. et al. (2019) Glacial lake evolution and Atlantic-Pacific drainage reversals during deglaciation of the Patagonian Ice Sheet. *Quatenary Science Reviews*, 203, 102–127.

Tjallingii, R., Stattegger, K., Wetzel, A. & Van Phach, P. (2010) Infilling and flooding of the Mekong River incised valley during deglacial sea-level rise. *Quatenary Science Reviews*, 29, 1432–1444.

Turner, K.J., Fogwill, C.J., McCulloch, R.D. & Sudgen, D.E. (2005) Deglaciation of the eastern flank of the north patagonian icefield and associated continental-scale lake diversions. *Geogr. Ann.: Ser. A Phys. Geogr.* 87, 363–374.

van den Boogaart, K.G. & Tolosana-Delgado, R. (2008) "composition": A unified R package to analyse compositional data. *Computers & Geosciences*, 34, 320–338.

Viana, A.R., Faugères, J.-C. & Stow, D.A.V. (1998) Bottom-current-controlled sand deposits—a review of modern shallow-to deep-water environments. *Sediment. Geol.* 115, 53–80.

Violante, R.A. & Parker, G. (2004) The post-last glacial maximum transgression in the de la Plata River and adjacent inner continental shelf, Argentina. *Quat. Int.* 114, 167–181.

Violante, R.A., Paterlini, C.M., Marcolini, S.I., Costa, I.P., Cavallotto, J.L., Laprida, C. et al. (2014) The Argentine continental shelf: morphology, sediments, processes and evolution since the Last Glacial Maximum. *Geol. Soc. London, Mem.* 41, 55–68.

Weber, N., Chaumillon, E., Tesson, M. & Garland, T. (2004) Architecture and morphology of the outer segment of a mixed tide and wave-dominated incised valley, revealed by HR seismic reflection profiling: The paleo-Charente River, France. *Marine Geology*, 207, 17–38.

Weltje, G.J. & Tjallingii, R. (2008) Calibration of XRF core scanners for quantitative geochemical logging of sediment cores: theory and application. *Earth and Planetary Science Letters*, 274, 423–438.

Zaitlin, B.A., Dalrymple, R.W. & Boyd, R. (1994) The stratigraphic organization of incised-valley systems associated with relative sea-level change. SEPM Spec. *Publ*, 51, 45–60.

Zanchetta, G., Consoloni, I., Isola, I., Pappalardo, M., Ribolini, A., Aguirre, M. et al. (2012) New insights on the Holocene marine transgression in the Bahía Camarones (Chubut, Argentina). Ital. *J. Geosci.* 131, 19–31.

Zanchetta, G., Bini, M., Isola, I., Pappalardo, M., Ribolini, A., Consoloni, I. et al. (2014) Middle- to late-Holocene relative sea-level changes at Puerto Deseado (Patagonia, Argentina). *The Holocene*, 24, 307–317.

Zecchin, M., Catuneanu, O. & Caffau, M. (2019) Wave-ravinement surfaces: Classification and key characteristics. *Earth Sci. Rev.* 188, 210–239.